

Visualization of the interaction of solutions
through a microfluidic chip using Terahertz
technology

February, 2021

Feroz AHMED

Graduate School of
Natural Science and Technology
(Doctor's Course)

OKAYAMA UNIVERSITY

DOCTORAL THESIS

Visualization of the interaction of solutions through a microfluidic chip using Terahertz technology

Author:

Feroz AHMED

Supervisor:

Toshihiko KIWA

Co-supervisors:

Kazuhiro FUJIMORI

Keiji TSUKADA

A dissertation submitted to

OKAYAMA UNIVERSITY

in partial fulfillment of the requirements for the degree of

Doctor of Philosophy in Engineering

in the

Graduate School of Natural Science and Technology

February 16, 2021

TO WHOM IT MAY CONCERN

We hereby certify that this is a typical copy of the
original Doctoral dissertation of

Feroz AHMED

Thesis Title:

Visualization of the interaction of solutions through a
microfluidic chip using Terahertz technology

Signature of Supervisor

Professor Toshihiko KIWA

Declaration of Authorship

This dissertation and the work presented here for doctoral studies were conducted under the supervision of Professor Toshihiko Kiwa. I, Feroz AHMED, declare that this thesis titled, “Visualization of the interaction of solutions through a microfluidic chip using Terahertz technology” and the work presented in it are my own. I confirm that:

Signed: Feroz AHMED Student number: 51429651

Date: February 12, 2021

Abstract

Feroz AHMED

Visualization of the interaction of solutions through a microfluidic chip using Terahertz technology

Terahertz (THz) waves are electromagnetic waves with frequency components between 100 GHz and 10 THz, shows exclusive spectral features such as a non-ionizing nature, high spatial resolution, good penetration capabilities etc. that make this technology to exhibit its impact on many applications of spectroscopy, sensing, and imaging processes. Therefore, THz wave radiation shows its sensitivity to the chemical solutions, cells, and tissues with different water contents. In addition, THz imaging technique can reveal the orientation of a hydrogen bond owing to its intermolecular bonding. THz radiation gradually decreases when it travels through any medium with a high water concentration. As a result, THz wave can distinguish even small fluctuations in the water contents of chemical and biological solutions for identifying and capturing the interaction of different chemical and biological solutions like pH solutions, DNA, enzyme, tissue and blood samples etc. In the commercial market, a charge-coupled device (CCD) camera is available to capture the images of biological and chemical reactions. However, this CCD camera does not be able to capture the images of the interaction of molecules inside the chemical and biological solutions satisfactorily. Whereas, THz image sensing technology is the recent advancement in the lab-on-chip technology to visualize and capture the images of chemical interactions of pH buffer solutions, blood, tissues, enzyme, DNA and so on in detail

without the use of any fluorescent dye marker which makes it reliable label-free detection and visualization technique. Even microfluidic channels made from different materials are opaque in the visible and near-infrared domains, THz technology is functioning effectively.

In this research, a sensing plate was fabricated as a part of using a sensor. The sensing plate consists of SiO_2 and Si film on a sapphire substrate. Terahertz waves were generated from the Si layer in the sensing plate when the femtosecond laser is irradiated to the bottom side of the sensing plate through the sapphire substrate. Electrons jumped into the conduction band from their excitation because they absorbed photons of generated femtosecond laser pulses whose bandgap energies are higher than the bandgap energies of silicon layer. The magnitude of the depletion field depended on the electric potential at the surface of the sensing plate. And, the amplitude of the radiated terahertz waves depended on the magnitude of the depletion field. Thus, the interaction of different concentrations of pH buffer solutions through microfluidic channels was connected to the electric potential on the sensing plate and such interaction of concentrations of different pH solutions was able to visualize by measuring the amplitude of radiated THz waves.

Viscoelastic material PolyDiMethylSiloxane (PDMS) can be one of promising candidates for the fabrication of microfluidic chip (MC) in micro scale for a wide range of applications in biological and medical research. Therefore, PDMS can be used for fabricating cost effective microfluidic chip with different microfluidic channels owing to its excellent properties of optical transparency, easy and swift fabrication process, chemical inertness and low shrinkage rate with the replication of the mold into the micro-scale environment. Moreover, without requiring expensive clean room facilities with time consuming fact, CAD designed 3D printed structure fabricated the replica mold of the microfluidic chip using PDMS. For preparing the PDMS microfluidic chip, cross-linked two agents

of Sylgard 184 Silicone elastomer base agent and Sylgard 184 Silicone elastomer curing agent as an adhesive were employed. Two inlet wells and one outlet well based a 3D structure of a microfluidic chip was drafted using a student version Solid work software, translated it into STL format and then printed the structure from the high definition 3D printer. PDMS sample made microfluidic chip was developed by cross-linking both the base and curing agents at a mass ratio of 10:1. Then, 3D printer printed the designed structure of the microfluidic chip and the cross-linked solution was poured into that printed structure for preparing replica mold of PDMS chip. PDMS was then put into the oven for 24 hours in a controlled 40 degrees Celsius. When it became hard enough, PDMS was used to design the microfluidic chip for the experiment.

The nature of internal fluid flow parameters through a microfluidic chip can be revealed using Terahertz (THz) image sensing technology and ANSYS fluent simulation to evaluate the chemical and biological samples in the micro scale level for the advancement of next healthy generation. Therefore, the trace of internal microfluidic reactions of chemical and biological solutions through a microfluidic chip from both the experimental and simulation-based analyses is a much expected trend to a fluid flow design and estimation engineer in the research and development field for serving the society with the proposed THz technology. In this doctoral dissertation, two inlet wells and one outlet well based, capillary concept a microfluidic chip was designed, and evaluated in terms of its internal performance of microfluidic parameters from fluid dynamics (FD) and its response to the experimental and simulation works. As a part of applied samples for the testing and analysis purpose, two pH=4 and 10 buffer solutions (BS) were injected through the internal micro flow channels (MFC) of the designed microfluidic chip in the above mentioned cross-disciplinary areas. Then, THz laser started to scan the interaction of the mixed solutions for the trace of internal microfluidic reactions by capturing THz images which was

directed by the THz chemical microscope (TCM) of our laboratory. Hence, this fabricated microfluidic chip can detect any imbalanced condition of pH level of human bodies out of metabolism, respiration processes, pH control of liquid foods of food industries for the development of biomedical applications in a wide range.

This dissertation also includes the proposed design of an adaptive digital filter in LABView simulation to reduce the internal noises during the optical signal to electrical signal conversion procedure of the project. The outcome of this dissertation was to improve the contrast and resolution of the THz images without losing the original speed of laser scanned THz images. This filter helped to scan THz images without losing the original speed of TCM with the reduction of total measurement time of the lock-in-amplifier which was connected with the entire THz signalling and imaging system. Thus, the integration of the above mentioned filter with the TCM system can provide the guideline of faster captured images technique with the faster scanning of samples like movie clips, quick occurred chemical reactions etc. in future.

In this dissertation, from the proposed capillary designed microfluidic chip with different dimensional paths of cylindrical shaped channels along with the traditional rectangular channels, it was calculated all microfluidic resistances through the micro flow channels and revealed the variation of internal fluidic parameters to evaluate the performance of the microfluidic chip experimentally. Microfluidic internal parameters like pressure drop, velocity, fluid flow rates of the mixed two pH 4 and 10 buffer solutions were measured and calculated to find out the characteristics of all microfluidic parameters. In addition, ANSYS fluent 2D simulation was also performed for the trace of internal interactions of pH buffer solutions through the designed microfluidic chip. Then, experimental results were validated with the obtained simulation results to emphasize the results in terms of fluid dynamics.

Acknowledgements

It was my long cherished desire to do Doctoral research and here in Okayama, I have been passing the best part of my academic career since my enrollment here as a PhD student on October, 2017. My heartfelt gratitude to many persons who directly and indirectly helped me to finish such gigantic research work to find a good outcome.

In this marathon journey of my doctoral research work, first of all, I would like to express my heartfelt gratitude to my honorable PhD thesis supervisor, *Professor Dr. Toshihiko Kiwa*, Faculty of Interdisciplinary Science and Engineering in Health Systems, Department. of Medical Bioengineering of Okayama University, Japan who motivated me to explore in this new terahertz field enthusiastically with the chance of work at his laboratory (*Advanced Electro Measurement Technology Laboratory*) in versatile ways to establish new ideas during my research period. I am also grateful for his ceaseless supervision, innumerable counseling, and unrelenting conviction. Honestly speaking, I passed and enjoyed three and half years huge productive time under the supervision of my supervisor to enrich my individual profile and gain effective knowledge with the confident feeling as a young researcher to fix my future endeavour. His counseling and expertise in the field showed me the perfect guideline and path to overcome many difficulties that I encountered during my studies under his supervision. I am grateful to *Kiwa Sensei* for his advice and invaluable suggestions in all aspects of my research and beyond research activities. This dissertation would not have been come into being without his inspiration and relentless

encouragement.

I would like to give my special thanks to my co-supervisor Professor Dr. *Keiji Tsukada* (*Advanced Electro Measurement Technology Laboratory*) who first forwarded my PhD seeking email to my PhD thesis supervisor. Then, my heartiest thankfulness goes to Associate Professor, Dr. *Kenji Sakai* (*Advanced Electro Measurement Technology Laboratory*), (*Advanced Electro Measurement Technology Laboratory*), Faculty of Interdisciplinary Science and Engineering in Health Systems, Department. of Medical Bioengineering of Okayama University, Japan, who gave me the logistic and academic support in parallel with my honorable supervisor. My forever gratefulness to my Master thesis supervisor, *Professor Dr. Mauricio Moreno Sereno*, Integrated Optics Laboratory, Department of Electronics, University of Barcelona, Spain who recommended strongly for my PhD admission here at Okayama University, Japan. My Master thesis supervisor guided me intensively during my Master thesis defense to be defended it successfully. I would like to express my heartfelt gratitude to *Professor Dr. Ramon Villaseca*, ex-coordinator of International Master of Europhotonics program, present emeritus professor, Department of Physics, Polytechnic University of Catalonia, Barcelona, Spain who taught me Introduction to Photonics, Optics, Laser course during my study in Master program. I learnt and inspired a lot from his lectures into the Master classes. He guided me so well whenever I needed to learn anything precisely and clearly of his course. I am highly obliged and thankful to my co-supervisor, Associate Professor Dr. *Kazuhiro Fujimori* (*Optoelectronics and Wave Engineering Laboratory*) for having his time to go through my thesis draft. I would like to express my gratefulness to Assistant Professor, Dr. *Jin Wang*, (*Advanced Electro Measurement Technology Laboratory*), Faculty of Interdisciplinary Science and Engineering in Health Systems, Department. of Medical Bioengineering of Okayama University, Japan, for going through my thesis draft thoroughly and advised me a lot from his experiences.

Then, I would like to dedicate my such academic achievement to my parents for whom I am in this world. Also, my huge respect to my wife who motivated me during my hard time of this tenure of PhD research.

I am really grateful to my paternal grandfather, paternal uncle of my mother and maternal grandfather who left this world with their dreams to see me at the highest zenith of success in my academic career.

I am thankful to all my teachers at schools, college and universities levels both in my undergraduate and Masters programs who taught me to show such a prestigious path of the knowledge of ocean.

My heartfelt gratitude to my maternal two uncles who taught me good mathematics to utilize my expertise in the fields of Engineering and my younger brother who always gives me logistic support with his accompany to my parents at their old ages during my research time at abroad.

Thanks to Japanese scholarship organization *JASSO, Otsuka Toshimi Scholarship Foundation* and all funds provided by my supervisor and Okayama University, which helped to fulfil my long cherished dream to pursue my doctoral study in Japan.

I gratefully acknowledge all the funds that were afforded by my supervisor and research fund of Okayama University to join several international conferences in Japan as well as in abroad and conduct research activities.

My heartiest gratitude to all the administrative officers of the Graduate school of Engineering who directly or indirectly made an impact on my doctoral study.

I would like to express my special thanks to my seniors, juniors, and friends in the laboratory for creating a great work atmosphere and their generous support. Specially, I always remember *Taiga Morimoto, Tatsuki Kamiya, Yuki Maeno,*

Atsuya Mahana, Minoru Hayashi, Yuichi Yoshida and so on for their nice gestures with me and all types of logistic support. And thanks again in general to all the laboratory members for the wonderful time I spent together with them.

I would like to express emotional gesture to the general people of my country, Bangladesh who paid the tax to the Republic of Government of Bangladesh to make me an engineer during my under graduate study. Without their relentless support, I did not become an engineer and can not continue my journey with such prestigious doctoral research environment in the abroad.

At last, I would like to tribute to all the Terahertz technology and Microfluidics involved researchers whose works in these fields to make good technological inventions for the sake of welfare of the society. Further, I would like to extend my thanks to all my research collaborators, co-authors, and reviewers for making a life time memorable journey during the period of my doctoral study.

Contents

Declaration of Authorship	v
Abstract	vii
Acknowledgements	xi
Contents	xv
List of Figures	xix
List of Tables	xxiii
List of Notations and Symbols	xxv
Research Activities	xxix
1 Introduction	1
1.1 Use of THz Chemical Microscope (TCM) to utilize THz Technology in this research	3
1.1.1 Reasons of the use of THz Technology over other technologies	4
1.1.2 Noises Involved in THz Signals and Images Processing	5
1.1.3 Applied Digital Filter in THz Technology	5
1.2 Fluid Dynamics in Microfluidics	6
1.2.1 The Speciality of the Designed Microfluidic Chip over other Conventional Microfluidic Chips	7
1.3 Outline of this Thesis	8
1.4 Motivation	10
2 Mechanism of THz Imaging	11
2.1 THz generation principle	12
2.2 THz detection principle	13
2.3 Experimental set up of TCM	15

2.4	Characteristic Curve Analysis from the Experiment	16
2.5	Summary	18
3	PDMS designed Microfluidic Chip	19
3.1	Preparation of PDMS	20
3.1.1	Top and bottom plates design to squeeze PDMS	22
3.1.2	Cross-sectional view of designed micrfluidic chip and isometric view of central main structure of microfluidic chip	23
3.1.3	Advantages and key features of PDMS	23
3.1.4	Summary	24
4	Microfluidic Parameters Measurement, Calculation and Statistical Analysis	29
4.1	Introduction	29
4.2	Mathematics	29
4.3	Calculation of Microfluidic Resistances of Microfluidic Chip . . .	31
4.4	Pressure Drop Measurement and Velocity Profile Estimation from Fluid Dynamics	36
4.5	Summary	42
5	Simulation to Emphasize the Experimental Result	43
5.1	Introduction	43
5.2	Simulation Algorithm	44
5.3	Mesh dependency and validation of simulation in CFD environment	51
5.3.1	Mesh dependency and validation of simulation	51
5.4	Summary	53
6	Digital Filter Design and Testing	55
6.1	Introduction and Motivation	55
6.2	Working Principle of an Adaptive Digital Filter	55
6.3	Experimental Set up for ADF's Proper Functioning Check . . .	57
6.4	Statistical Analysis of Characteristic Curve of ADF	59
6.5	Determination of Contrast of THz Images	61
6.6	Qualitative Analysis of Contrast with and without Filter	62
6.7	Contour of THz Images with and without Filter	63
6.7.1	Data Acquisition of THz Images	64
6.8	Advantages of an Adaptive Digital Filter	65
6.9	Summary	65
7	Results and Discussions	67

7.1	Introduction	67
7.1.1	THz Imaging results	69
7.1.2	2D ANSYS Fluent simulation results	70
7.2	Analysis of Velocity Profiles obtained from ANSYS Fluent	72
7.3	Summary	73
8	Conclusion and Future Works	75
	Bibliography	79
	Biography	95

List of Figures

2.1	The sensing plate for the TCM system with three different layers fabricated sensing chip	11
2.2	THz electromagnetic waves generation with the irradiation of femto second laser pulses onto the layers of the sensing chip . .	12
2.3	THz electromagnetic wave's detection to capture the pH buffer solutions interaction	13
2.4	Optical part arrangement of the TCM system for this project . .	14
2.5	Whole THz signaling system to convert the optical signal to electrical signal with a two stage controlling mechanism	15
2.6	By applying THz electromagnetic wave, buffer solutions at pH values of 4 and 10, injected through two inlet wells via syringe-connected tubes and flushed out through the outlet well	17
2.7	Characteristic curve of THz response with respect to different pH concentration values	18
3.1	Different dimensions of micro flow channels' 3D lay out in Solid work.	19
3.2	3D-printed structure of the microfluidic chip with dimensions of 20 mm × 20 mm scaling in Solid work	20
3.3	practical 3D printed structure for preparing replica of this structure	21
3.4	Hard replica mold within 3D printed structure	22
3.5	Manual cut microfluidic chip attached with Si: sapphire glass substrate (clipped with bottom 3D printed plate)	23
3.6	Bottom plate designed in CAD software (In the middle, Si:sapphire glass substrate of 10 mm × 10 mm was clipped and PDMS-made MC was attached with glass substrate	24
3.7	Top plate designed in CAD to squeeze the microfluidic chip with glass substrate and bottom sensing plate	25
3.8	Top view of internal micro fluidic channels formation in Solid works using different internal designed dimensions	25

3.9	Microfluidic chip that attached with Si:sapphire glass substrate, screwed and tilted in a balanced way to squeeze it with top and bottom plate	26
3.10	cross-sectional view of designed 3D structure	26
3.11	Scaling in solid work of main microfluidic chip's lay out along with micro flow channels	27
4.1	Digital pressure machine (DPM) controlled fluids flow through a capillary design based microfluidic chip	32
4.2	Internal rectangular, cylindircal resistances calculation of the desinged microfluidic chip	33
4.3	Different internal dimensional microfluidic wells of the microfluidic chip	34
4.4	Equivalent MFR calculation to find out resultant fluid flow rate and pressure drop of entire microfluidic chip	35
4.5	Estimation of average pressure drop across the points of two inlet wells using set values of fluid flow rates.	39
4.6	Quantitative data analysis of average pressure drop across the point of only outlet well using experimental measured values of fluid flow rates.	40
4.7	Statistical data analysis of average velocity versus fluid flow rate through the outlet well	41
4.8	Statistical data analysis of average velocity versus fluid flow rate through the two inlet wells of same designed diameter in dimension	42
5.1	Exact dimensional 3D structure formed in ANSYS simulator to run the program with different microfluidic paramters of fluid dynamics	44
5.2	Validation of numerical model with experimental data for pressure drops at inlets and outlet	48
5.3	Flowchart of 2D ANSYS Fluent simulation using fluid dynamics	50
5.4	Mesh dependency for grid-independent study of validation . .	52
6.1	Functionality of an ADF during the computational operation . .	56
6.2	Sensing plate arrangement for the testing of effectiveness of the ADF	57
6.3	Conceptual diagram of four wells plate with the application of THz wave	58
6.4	Optical set up of TCM system to start measurement for this project	59

6.5	Standard deviation versus step size curve for evaluating the characteristics of 100 ms and 30 ms TC of lock-in-amplifier with the application of ADF	60
6.6	Calculation and estimation of standard deviation for several pixels of data of THz images inside the upper of the well and outside region of the Well onto sensing plate	62
6.7	Contour of THz Image with filter for the contrast of 0.73, TC 100 ms	63
6.8	Contour of THz Image without filter for the contrast of 0.32, TC 100 ms	63
6.9	Contour of THz Image with filter for the contrast of 0.74, TC 30 ms	64
6.10	Contour of THz Image without filter for the contrast of 0.34, TC 30 ms	64
7.1	THz captured data for the interaction of pH 4 and 10 buffer solutions at 0.07 mL/min fluid flow rate	68
7.2	THz captured data for the interaction of pH 4 and 10 buffer solutions at 0.15 mL/min fluid flow rate	68
7.3	THz captured data for the interaction of pH 4 and 10 buffer solutions at 0.25 mL/min fluid flow rate	69
7.4	THz captured data for the interaction of pH 4 and 10 buffer solutions at 0.4 mL/min fluid flow rate	69
7.5	THz captured data for the interaction of pH 4 and 10 buffer solutions at 0.7 mL/min fluid flow rate	69
7.6	THz captured data for the interaction of pH 4 and 10 buffer solutions at 0.8 mL/min fluid flow rate	69
7.7	Same set of input velocity applied to each of two inlet wells with respect to different increased volume of fraction; same input velocity, 0.064 m/s applied at A and B points for two pH solutions.	70
7.8	Same set of input velocity applied to each of two inlet wells with respect to different increased volume of fraction; same input velocity, 0.096 m/s applied at A and B points for two pH solutions.	71

List of Tables

4.1	Pressure drops through pH=4 inlet well for the certain ranges of set values of fluid flow rates from DPM	36
4.2	Average Pressure drop through pH=10 inlet well for the certain ranges of set values of fluid flow rates from DPM	37
4.3	Average pressure drop through outlet well from the experimental measured fluid flow rates	37
4.4	Average velocity through outlet well from the experimental measured fluid flow rates	38
4.5	Average velocity measurement through inlet wells using "set values" of the fluid flow rates of DPM	38
5.1	Measured Different Fluidic Parameters Given As Input Data And Calculated Input, Output Data.	45
5.2	Validation Of Experimental And Simulation Based Fluidic Parameters.	47
5.3	Setup Model and Solver conditions	49
5.4	Solution conditions	49
5.5	Calculation conditions	49
5.6	Mesh Dependency For Grid-Independent Study Of Validation Using Linear Regression Method	51
6.1	Estimation of Standard Deviation and Contrast of THz Images .	63

List of Notations and Symbols

Notation	Description
μ	viscosity of the fluid.
ρ	Density of the fluid.
R_e	Reynold Number.
p_{st}	Static pressure of the fluid.
∇	Vector differential operator.
F_{css}	Surface tension force.
α_1	Thermal Diffusivity.
h	Internal energy.
λ	Thermal conductivity.
μm	Wavelength of the light.
THz	High frequency Terahertz signal.
Q_n	Fluid flow rate.
ΔP_n	Pressure drop of the fluid.
R_f	Microfluidic resistance.
R_H	Hydrodynamic resistance.
D_{hh}	Characteristic length of a fluid.
E_q	For each phase, specific heat.
T	Temperature.

*Dedicated to all the persons who I owe the most. To my parents
for whom I am in this world, my wife and younger brother who
sacrificed the most during my journey in Doctoral research.*

Research Activities

Peer-Reviewed Journal Papers (First author)

1. **Feroz Ahmed**, Atsuya Mahana, Katsuya Taniizumi, Jin Wang, Kenji Sakai, and Toshihiko Kiwa “Terahertz imaging technique for monitoring the flow of buffer solutions at different pH values through a microfluidic chip”. In: *Japanese Journal of Applied Physics*, (2021), DOI: 10.35848.

Peer-Reviewed International Conference Papers (First author)

IEEE Xplore indexed:

2. **Feroz Ahmed**, Tatsuki Kamiya; Yuki Maeno; Toshihiko Kiwa; Kenji Sakai; Keiji Tsukada. “Improvement of contrast of Terahertz Images of a Terahertz Chemical Microscopy using Adaptive Digital Filter”. In: *2019 International Conference on Computer, Communication, Chemical, Materials and Electronic Engineering (IC4ME2)*, Bangladesh, 11-12 July 2019, pp. 1-4. DOI: 47184.2019.9036485.

Springer Published:

3. **Feroz Ahmed**, Partha Chakraborty, Md. Monirul Kabir, Md. Shahjahan, and Kazuyuki Murase. “An Automatic Speaker Recognition System”. In: *International Conference on Neural Information Processing (ICONIP) 2007*, Japan, 2007, pp 517-526. DOI:10.1007.

Chapter 1

Introduction

When God said “Let there be light”, He surely must have meant perfectly

coherent light and photons. – Charles Townes

Terahertz (THz) - the electromagnetic wave with the frequency components between 100 GHz and 10 THz, possesses extra ordinary spectral features of its radiation, namely non-ionizing [Yan+16], [Dan+19], non-invasive [Yan+16], [Dan+19], phase-sensitive to polar substances [Dan+19], [PMW09], penetration capabilities [Yan+16] through non-polar molecules, high spatial resolution [Dan+19],[NP+17] etc. which show the scenario of this technology with higher significance in case of applications in spectroscopy [PZ15], [He2] sensing [Zho+19] and imaging [Sta+20] processes. Therefore, chemical solutions, cells and tissues with different water contents exhibit with the distinctive responses to the radiation of THz wave. Moreover, the trace of the orientation of hydrogen bond due to its intermolecular bonding can be revealed by THz imaging technology. THz radiation is gradually diminished as one of its important characteristics when it travels through a medium with an increased water concentrations. Therefore, it can distinguish even small fluctuations in water contents of chemical and biological substances like pH buffer solutions, tissues [He2], blood [Jeo+13] etc. which make THz vital technology for revealing and capturing the interaction, chemical reactions of different chemical

solutions and abnormal cell divisions inside the tissues to detect cancer cells and so on. Therefore, it is possible to capture the internal microfluidic reactions of the microfluidic chip using THz laser scanning in the form of THz images with the detailed maps of chemical and biological reactions.

Microfluidics system [SW03; BMW02] is one of emerging solutions for the miniaturization of biological [SW03; Bur02; MH02] and chemical assays since its enrollment in the field of biomedical engineering. Its feature of small scale integration enables it to capture the targets like detection of proteins [BMW02; Ver02; Slo+05], cell sorting and analysis [CK07; BLL06; Che+08; Sal+10], nano-particles [Par+17; Kel+08], cells [GYF04], DNA detection and amplification [Dor+05; Eas+06], germs [Wan+18], chemical ions and so on within the short internal structural distances to make electric or magnetic fields more useful for sensing and detecting the above mentioned all objects. The structures of modern microfluidics are capable of miniaturizing or integrating traditional laboratory practices by making lab-on-chips devices for the sake of reducing time and saving cost [Sai+11a].

At the microscale level, microfluidic devices [YII18] utilize the physical and chemical properties of liquids and gases. They come into being with several benefits over the others existing conventional sized systems. Moreover, microfluidic devices permit the analysis and use of less volume of samples, chemicals and reagents to decrease the global fees of applications . Many operations can be implemented at a time with the excellent features of their compact sizes, shortening the time during the experiment. In addition, their features contain an excellent data quality and substantial parameter control which permit the process of automation while preserving the performances of them. Moreover, they have the capability to both process and analyze the samples with minor sample handling. Microfluidic chips are expanded so that the incorporated automation permits the users to generate multi-step reactions with the requirements

of a low level of expertise and multi-functionalities. The eye-catching services like faster reaction time, enhanced analytical sensitivity, enhanced temperature control, portability, easier automation and the integration of lab routines in the lab-on-a-chip devices make microfluidics versatile for the diverse uses in chemical and biological research. The manufacturing materials of microfluidics are cheap as they do not involve with the use of various costly equipments.

1.1 Use of THz Chemical Microscope (TCM) to utilize THz Technology in this research

In the method of THz Time-Domain Spectroscopy (TDS) , the amplitude and phase of short-pulsed incident THz (i.e., 10^{12}Hz) radiation show the high sensitivity to the properties of materials of a sample. Therefore, some particular imaging systems which utilize THz TDS, are suitable for the applications [Ton07] of all novel nondestructive testings (NDT) [Kiw+03] . However, the spatial resolution of such systems which is about $300\mu\text{m}$ at 1THz, is so far limited by the wavelength of the THz radiation.

By considering the above mentioned fact, a laser-THz emission microscope (LTME) was proposed and developed for NDT of semiconductor devices like in the large-scale integrated circuits and solar panels [Yam+05; Kiw+03]. One of important features in terms of the spatial resolution of the laser-THz emission technique is that its spatial resolution is not limited by wavelength of the THz radiation, only limited by the wavelength of the femtosecond (i.e., 10^{-15}s) laser pulses that is utilized to generate the THz radiation. As a result, comparing with a conventional THz imaging system, higher spatial resolutions can be achieved using an LTME [KST13]. From this concept of sharp spatial resolution criteria and advantages of THz technology, my laboratory developed a

THz chemical microscope (TCM) which is used to visualize, capture and monitor the chemical, biological and/or electrical potential shifts caused by chemical reactions in detail. In my PhD research, I used such TCM based THz technology to utilize its impact on my designed microfluidic chip with the explanation from fluid dynamics. Besides, a digital filter was integrated with the THz controlling system to check the acceptable visibility of the brightness of contrast of THz images using the above mentioned TCM.

1.1.1 Reasons of the use of THz Technology over other technologies

The traditional image captured cameras do not have the full satisfactory features to visualize the internal chemical and biological reactions inside the microfluidic chips [Ahm+21] convincingly. Comparing with the application of charge coupled device (CCD) cameras available in commercial markets for capturing the images of the interaction of chemical and biological reactions inside the microfluidic chips, the use of THz image sensing technology is the latest version as one of important value added services in lab-on-chip technology for visualizing and capturing of the image maps of chemical and biological reactions. Thus, the breakthrough of the above mentioned novel THz imaging technique is evident with the visualization, detection and capturing of chemical reactions of different pH buffer solutions without using any fluorescent dye marker. Therefore, such technique is regarded as a reliable label free detection and visualization technique. THz technology can be effective though the microfluidic channels fabricated from different materials which are opaque in visible and near-infrared domain. That means; they do not show the transparency in light. In the long run, from my designed microfluidic chip, for the fabrication of more moderate versions of the microfluidic chips, choice of materials or extension of properties of materials can be possible to add by experimenting the degree of effectiveness

of THz technology in a wide scale range for the sake of the progressive reports on chemical and medical research.

1.1.2 Noises Involved in THz Signals and Images Processing

In THz image sensing technique, there are two types of components of noises [Han+06] existed. One is signal noise and another one is imaging noise. The signal noise is responsible for the deformation of THz pulses in some unwanted ways, as opposed to the noise which an artifact of the process of imaging. On the contrary, imaging noise is associated with the noise for example; the incoming analogue signal was sampled by the Analog-to-Digital Converter (ADC) via the lock-in-amplifier where definitely the generation of noises in a process which invariably resulted in a digital approximation of the original analogue signal in spite of the presence of a low pass filter inside the lock-in-amplifier . Moreover, the alignment of each of optical instruments specially the alignment of pumping and trigger beams of THz signal were done by the human made controlling which in turn have the possibility of not maintaining the alignment always in a perfection mood. As a result, imaging noise might be occurred. To overcome different types of regular and irregular noises associated with the optical to electrical converted signal, it was necessary to design a compatible digital filter to handle such noises and reduced the noises to ensure the higher resolution and contrast based processing of THz images.

1.1.3 Applied Digital Filter in THz Technology

From the experiences of the existence of different noises involved in THz pulsed imaging technique, an Adaptive Digital Filter (ADF) was designed [Ahm+19] and integrated with the central THz image sensing system. There was also another important objective hidden inside such type of designing filter. The

objective was the visualization of the chemical and biological reactions with higher THz imaging quality and higher scanning speed. Therefore, it was required to improve the contrast of the THz images with higher quality of images. I applied an ADF to the TCM system and evaluated the quality of images qualitatively. The outcome was effective to improve the imaging quality without losing the scanning speed of the TCM and improved the total measurement time of each of samples from THz scanning laser as well. This filter design and its integration to the TCM system have already opened the door to capture the imaging maps of faster spreading out of chemical, biological solutions and/or movie clip. Thus, a breakthrough of faster scanning procedure for the faster movement of chemical and biological solutions would be effective and the latest edition in our novel cutting edge research of THz image sensing technology.

1.2 Fluid Dynamics in Microfluidics

The growing demands of microfluidics systems create the opportunity in the research and development field vastly to analyze and visualize [HSR13] the internal fluid flow parameters inside the micro flow channels (MFC) of a microfluidic chip (MC) which is the essential phenomenon to ensure good quality based chemical and biological products for the betterment of next healthy generation. As a result, it is a huge expected trend to a fluid flow design and estimation engineer to characterize, optimize and evaluate the performance of the interaction of chemical and biological solutions through the MFC for the quality assurance in the microfluidic platform. In this research work, I designed and fabricated two inlet wells and one outlet well based a capillary [Ola+18] design concept based MC from 3D printing and polydimethylsiloxane (PDMS)-made mold. Two pH 4 and 10 Buffer Solutions (BS) were injected into the two inlet wells and flushed out through the only outlet well of the capillary designed MC to analyze internal fluidic parameters of mixed two viscous BS.

It was built up a microfluidic circuit network [Oh+12] from different dimensions of MFC and fluidic parameters used for the designed MC. From the basic concept of Fluid Dynamics (FD), the pressure drop profiles, velocity profile of mixed two pH buffer solutions through two inlet wells and one outlet well were calculated, plotted and analyzed to evaluate the performance of the capillary designed MC. At the end, the experimental results were validated by the 2D simulation applied to the above mentioned MC using ANSYS Fluent simulator and from simulated data, velocity in each portion of the MFC was analyzed.

1.2.1 The Speciality of the Designed Microlfuidic Chip over other Conventional Microfluidic Chips

Owing to the structures of smaller dimensions of the different internal MFC of MC, the flow of fluids through MFC exhibit the laminar [KCD16c] nature of fluids' flow. However, due to the complexities of the states of the mixture of fluids, when two or more different viscous fluids mix with each other through the MFC, it is obvious to simulate, visualize and analyze the flow patterns of fluids at each point of the internal flow channels of a MC for the characterization and optimization of the nature of flow of fluids and different internal dimensions of MFC. Therefore, we need to generate 2D simulation using ANSYS fluent simulator [BGP08; APA19] with the output of simple and precise able fluid flow patterned data influenced by the friction due to the viscosities of the fluids within the internal layers of MFC [UH+18] with the variation of different speeds of different fluids. Thus, the performance evaluation and optimization of different dimensions of internal MFC can be achieved by the analyses of characteristics of internal microfluidic parameters like pressure drops, velocities, viscosities, microfluidic resistances etc.

Compared to the increased demands of varieties of complex internal architectures' formed microfluidic chips, the conventional method for the control of

the flow profiles through the internal straight forward rectangular paths based microfluidic chips [Sai+11b] due to the linear behavior of hydrodynamic equations at low Reynolds number , is experiencing tremendous challenge. Moreover, many chemical and biological researches based on lab on chips require precise ideas of the samples of the fluids flow through different dimensional and patterned (rectangular paths , circular shaped cylindrical paths , common junction circular paths and, so on) areas with the sharp analyses based on both the experimental and simulation works. Therefore, we designed and fabricated a Y-shaped MC with different dimensional rectangular paths, cylindrical shaped circular wells, a common junction based circular path [GGBY16; BL17] to combine the flow of two fluids. As fluid flow design and estimation engineers, experimental and simulation works gave us the scope of the optimization of different dimensional shaped paths of different flow of fluids based on fundamentals of fluid dynamics [Lin+16]. As a result, we achieved the goal to optimize a symmetric two arms and a common mixed fluids provided MFC contained a Y-shaped MC due to its good response of handling the flow of fluids. Further, for the injected two pH 4 and 10 BS through the MC, experimental measurement data were used to calculate all hydrodynamic parameters via internal MFC using FD.

1.3 Outline of this Thesis

The remainder of this dissertation has been planned and structured as follows:

Chapter 2 describes and defines the fundamental concept of THz image sensing technology, the higher spatial resolution of that technology in comparison with conventional laser excited system, experimental optical set up of TCM system to use for the experiment with the microfluidic chip, THz signal flow graph of the TCM system, the mechanism of THz generation, detection principles.

Chapter 3 introduces the capillary designed concept based an MC, its fabrication and final replica mold formation for making experimental shaped polydimethylsiloxane (PDMS) based an MC, advantages of using such PDMS made MC.

Chapter 4 contains the mathematical expressions used for the calculation of internal microfluidic paramaters of the MC, using all hydrodynamic parameters, establishment of a microfluidic circuit network and calculation of parameters of such network with the determination of the nature of flow of different fluids through the MC.

Chapter 5 includes the characteristics curves of pressure drop profiles, velocity profile according to FD from the experimental result of the designed MC. Then it was simulated for the trace of fluidic patterns of two different pH BS through the MC in ANSYS Fluent simulator. This chapter also concludes the very important validation of experimental results from the analysis of simulation based results. This chapter also explains the results of the obtained data of THz scanned lasers. The main contribution of this chapter is to find the THz imaging data which were recorded for the different fliud flow rates (FFR) of two pH BS by evaluating the average peak amplitude data of THz with respect to different concentrations of different pH BS.

Chapter 6 presents the basic principle of ADF and its algorithim following least mean square (LMS) of digital signal processing technique. It also introduces the optical set up of TCM system to check the efficiency of ADF which was integrated with the central THz image processing system for monitoring and visualization.

Chapter 7 concludes the qualitative analysis of the designed ADF for the improvement of the contrast of THz images. Here for the evaluation of the performance of the ADF, mili-Q water was used as sample to determine the different parameters of ADF.

Finally, **Chapter 8** includes this dissertation along with an outline of the future works.

1.4 Motivation

The research trend on different patterned MFC are the concerned matter for the sharp analysis of blood, cell samples, chemical solutions for the early medical diagnosis of different patients in comparison with the conventional straight forward rectangular path MFC [Sai+11a] which actually motivated me to fabricate capillary design concept based differnet patterned channels like cylindrical or circular path channels, common junction circular channel and rectangular paths within an MC.

Moreover, for the reduction of noises from THz signal data, it was required to implement an universal digital filter in spite of a low pass filter integration with our optical to electrical conversion part of lock-in-amplifier. Thus, the central TCM system connected with analog-to-digital converter (ADC) and lock-in amplifier were required to deliver almost noises free THz images which motivated me to design and test an ADF with our central THz image controlling system.

Chapter 2

Mechanism of THz Imaging

This chapter recalls the mechanism of THz generation, detection principles, experimental optical set up of TCM system used to operate the designed microfluidic chip, THz signal flow graph of the TCM system. The details presented in this chapter, will be found in [Kiw+19; Kiw+07], [Ahm+19; Ahm+21].

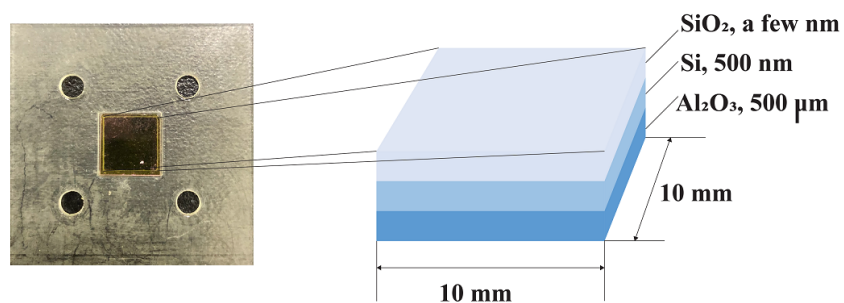


FIGURE 2.1: The sensing plate for the TCM system with three different layers fabricated sensing chip

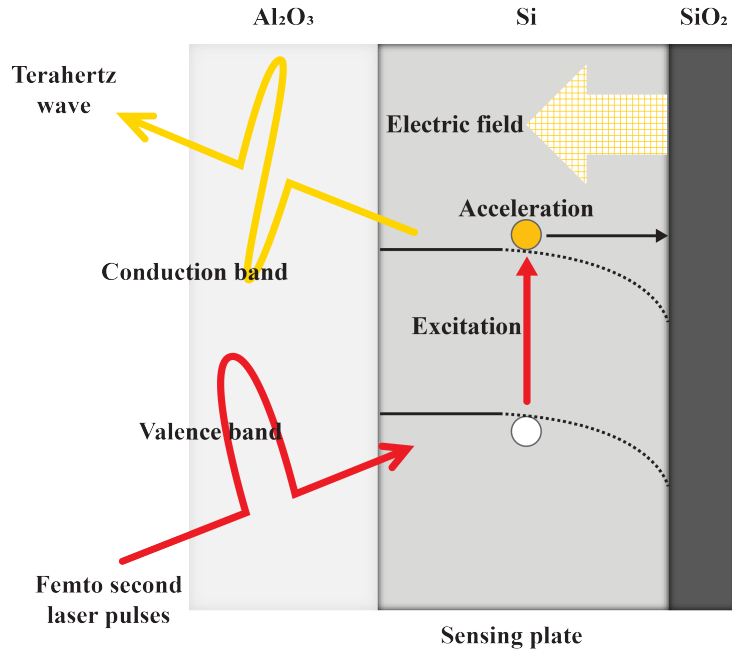


FIGURE 2.2: THz electromagnetic waves generation with the irradiation of femto second laser pulses onto the layers of the sensing chip

2.1 THz generation principle

To establish full set up of the TCM system, we used a sensing chip as a sensor, as shown in Fig. 2.1. It comprises of three layers of thin films of SiO_2 and Si deposited on a sapphire substrate. When the silicon layer was illuminated by femtosecond laser pulses of 800 nm wavelength from the sapphire substrate side, the electrons in the valence band was excited to jump to the conduction band, as shown in Fig. 2.2. An electron was excited to jump into the conduction band because it absorbed a photon of the femtosecond laser pulse, whose photon energy was higher than the bandgap energy of silicon. The dependency of the magnitude of the formed depletion region was on the electrical potential at the surface of the sensing plate. As a result, we can determine radiated THz wave's amplitude, which depended on the magnitude of the depletion field. When pH buffer solutions of different pH values like 1.68, 4, 6.86 and 10, flowing through the micro flow channels interacted on the sensing plate, the electric potential at the surface of the sensing plate and the amplitude of the radiated THz waves

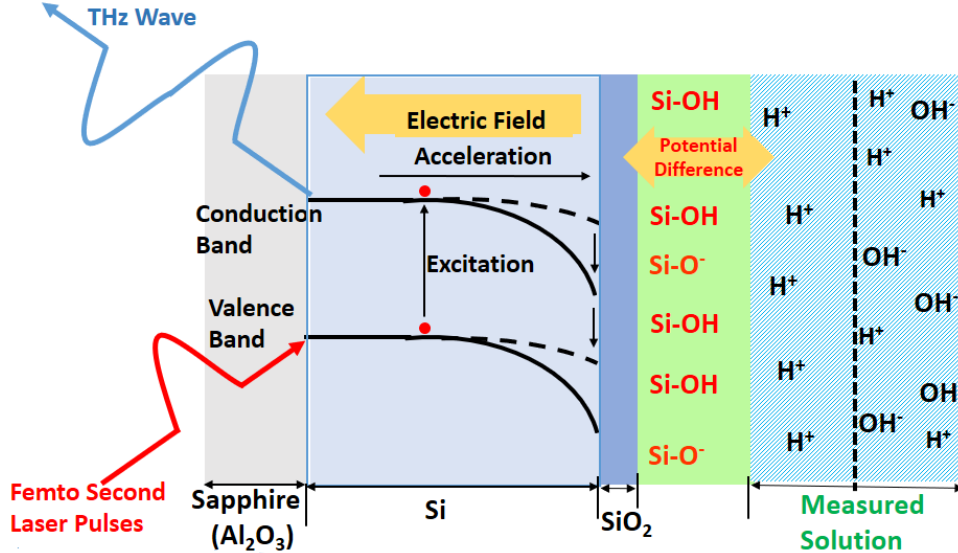


FIGURE 2.3: THz electromagnetic wave's detection to capture the pH buffer solutions interaction

were varied. As a result, a THz electromagnetic wave is proportional to the differential of the current density by the carrier acceleration that was generated according to 2.1.

$$E_{THz} \propto \frac{dJ}{dt} = e \frac{dn}{dt} \mu E_d S + en\mu \frac{dE_d}{dt} S \quad (2.1)$$

In 2.1, E_{THz} denotes the THz electromagnetic wave, J indicates the current density, e means the electric charge, n defines the photo-excited carrier density, S refers to the irradiated area of the laser spot, E_d symbolizes the surface electric field, and μ denotes the carrier mobility. Figure 2.2 depicts the generation principle of the terahertz waves that was originated from the sensing plate.

2.2 THz detection principle

In the project, THz laser was irradiated to the bottom side of the sensing plate through the sapphire substrate. Depletion field's magnitude depended on the electric potential at the surface of the sensing plate. And, the radiated terahertz

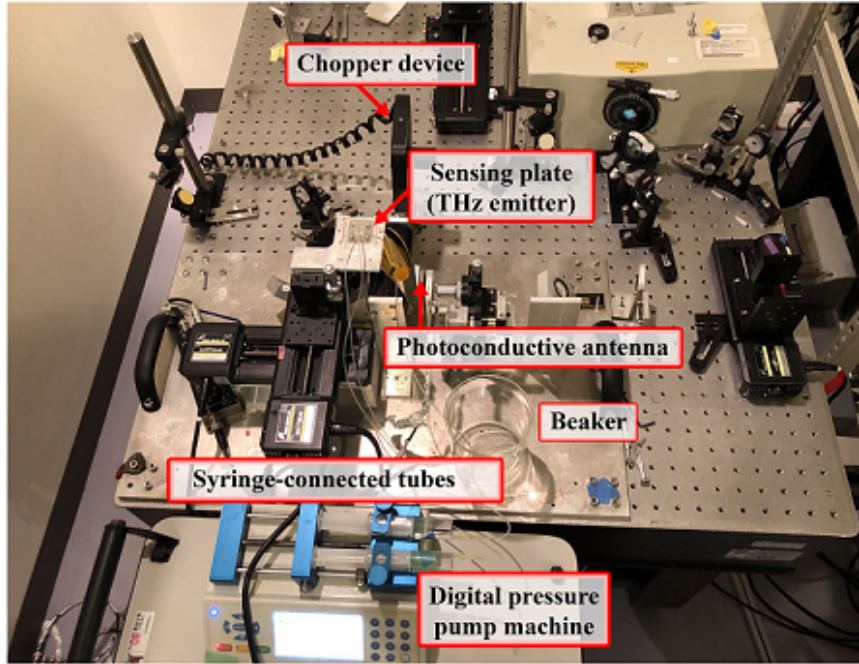


FIGURE 2.4: Optical part arrangement of the TCM system for this project

waves' amplitude depended on the magnitude of the depletion field. The chemical reactions of different concentration based pH buffer solutions occurred onto the sensing plate that led to the change in the electric potential at the surface of the sensing plate by detecting the interaction of the continuous flow of H^+ and OH^- ions based different pH buffer solutions. As a result, the concentration of H^+ and OH^- ions inside pH buffer solutions was able to be measured by measuring the amplitude of the radiated terahertz waves. TCM system measured the amplitude of THz waves that radiated from the sensing plate.

The H^+ ion concentration is higher than the OH^- ion concentration for acidic nature based pH solutions (4, 1.68, and 6.86). On the contrary, the OH^- ion concentration is higher than the H^+ ion concentration for a pH=10 buffer solution. In both cases, the H^+ and OH^- ions interacted with each other to reach chemical equilibrium that led to a potential shift on the surface of the sensing plate. This operation led to changes in the acceleration of the carriers. Therefore, generated terahertz wave's intensity also changed, and it was measured the interaction between different H^+ and OH^- ion concentrations from the change

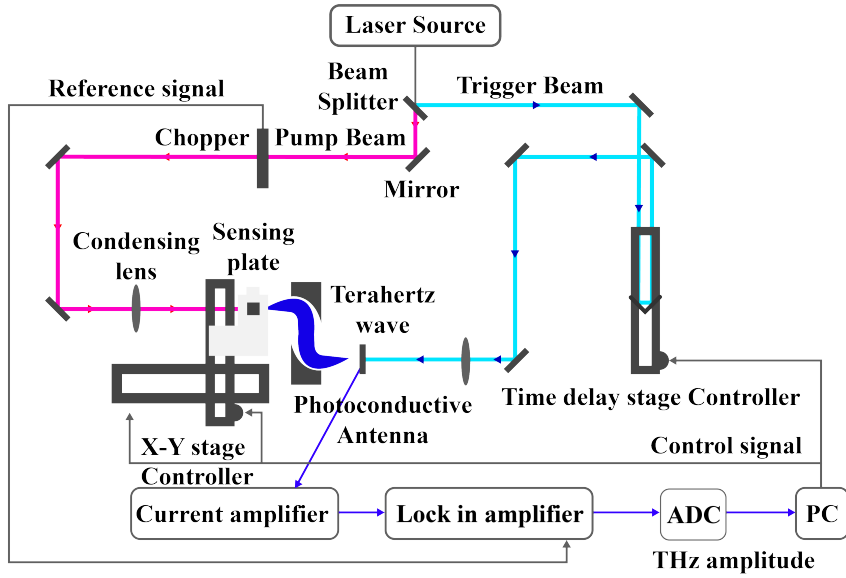


FIGURE 2.5: Whole THz signaling system to convert the optical signal to electrical signal with a two stage controlling mechanism

of the intensity of the THz amplitude. Figure 2.3 depicts the principle of THz detection .

2.3 Experimental set up of TCM

We selected a Ti: sapphire laser as a light source to develop a THz signaling system. 780 nm with a pulse width of 100 fs at the full width at half maximum was the center wavelength of the laser pulse. 790 W with a repetition rate of 82 MHz was the output of the laser system. We selected a digital pressure machine (DPM) connected to the two inlet wells of the microfluidic chip via two syringe-connected tubes for allowing the flow of different pH buffer solutions. The mixed pH solutions like pH 4, 1.68, 6.86, and 10, were flushed out spontaneously and stored into a beaker using another tube of 1 m from the outlet well. Figure 2.4 illustrates the experimental setup .

A THz detector detected the amplitude of the THz pulses. A bowtie-type photo-conductive antenna made by low-temperature-grown GaAs thin film, was selected as a detector. The peak amplitude of the THz wave was determined from the optical delay of the trigger pulses to the detector, that was fixed. a lock-in technique was employed for improving the signal-to-noise ratio (SNR) of the THz signal. To reduce the noise from the THz signal data, We selected a chopper (To synchronize the THz data, the frequency of the chopper was 2 kHz) in the lock-in technique. Furthermore, an adaptive digital filter (ADF) and an analog-to-digital converter (ADC) were programmed by a two-stage time delay controlling mechanism in LabVIEW® for improving the contrast of the THz images and sampling the THz signal data in a compatible manner based on the Nyquist sampling theorem. The THz signaling system in the form of a signal flow graph (SFG) shows the sequential architecture of its operation, as drawn in Fig. 2.5.

2.4 Characteristic Curve Analysis from the Experiment

During the experiment (Fig. 2.4), THz data of the interaction of two pH = 4 and 10 buffer solutions were captured and plotted as the contour of the THz images with respect to different fluid flow rates (viz: 0.07, 0.15, 0.25, 0.4, and 0.6 mL/min etc.) of digital pressure machine that applied to each of the two inlet wells of the designed microfluidic chip, driven by a THz laser-scanned TCM system.

The averaged data of the THz amplitudes with respect to different concentrations of the pH value are plotted in Figs. (2.7 and 2.6) using the programmed average [Ahm+19] raw data of the contour images of THz from the experimental measurement. To measure and evaluate such raw THz data, a total area

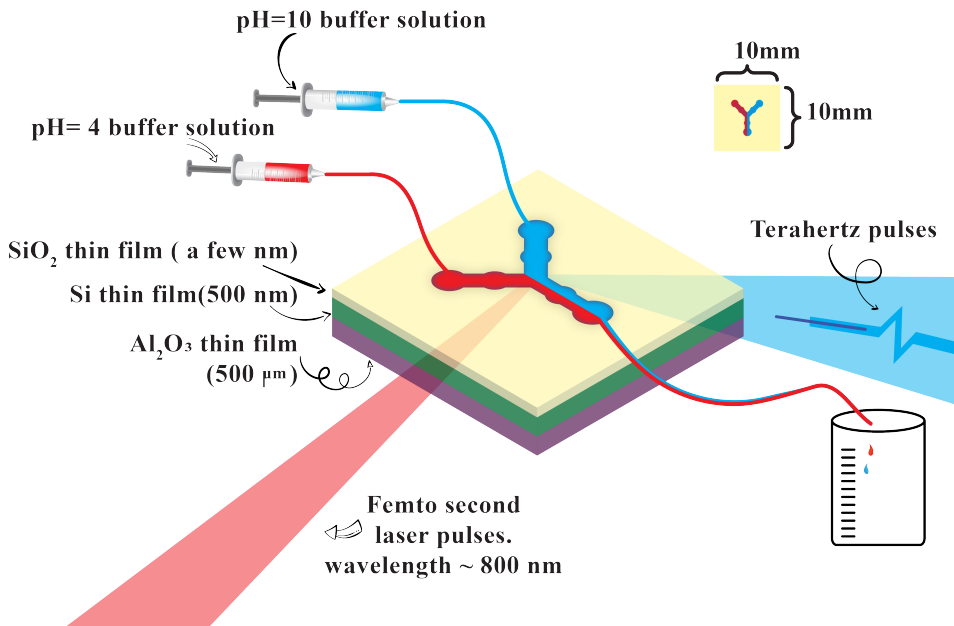


FIGURE 2.6: By applying THz electromagnetic wave, buffer solutions at pH values of 4 and 10, injected through two inlet wells via syringe-connected tubes and flushed out through the outlet well

of laser scanned of 10 mm × 10 mm was programmed in LabVIEW® by averaging the lock-in-amplifier data over the total measurement time [Ahm+19]. The characteristic curve denotes the criteria of the peak values of the THz data, that increased monotonically with the increased values of the pH concentration. Meanwhile, from the THz generation and detection principles (Figs. 2.2 and 2.3), the negative value of pH = 1.68 in Fig. 2.7 can be realized significantly, where a downward or reverse shift in the depletion layer indicated the potential shift in the depletion region, which led to a negative peak amplitude of the THz data. This sensitiveness of the TCM to pH values proved the quantitative measurements of the pH values via the micro flow channels of the designed microfluidic chip. In this way, even a small variation in the pH level can indicate the sensitiveness of THz amplitudes data to different pH levels data with the interaction of the pH values through the microfluidic chip, where the applications of pH buffer solutions is of great interest.

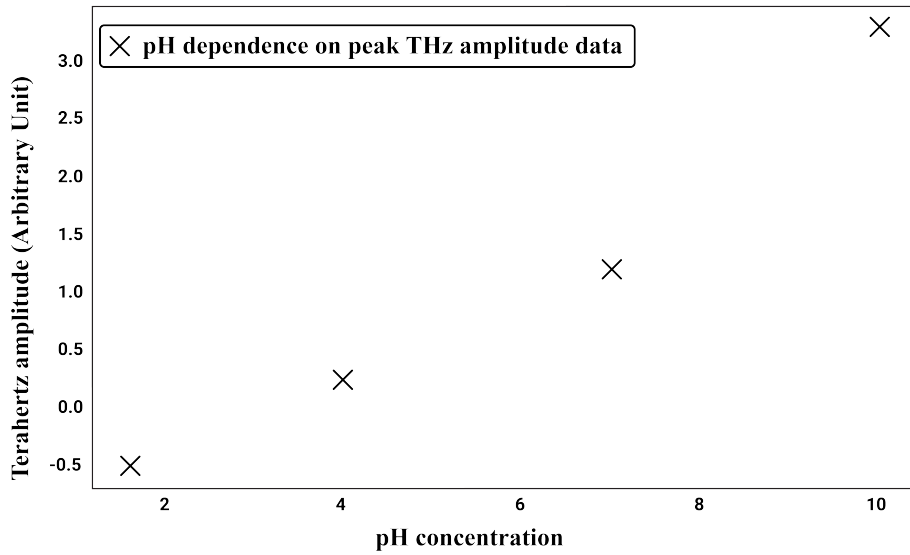


FIGURE 2.7: Characteristic curve of THz response with respect to different pH concentration values

2.5 Summary

This chapter defined the fundamentals of TCM system system's hardware set up, its mechanism followed by working principles of advanced physics and engineering. Moreover, the measurement and experimental data obtained from THz image sensing technology revealed the effectiveness of THz laser scanning in order to capture the internal microfluidic reactions by showing variations in different buffer solutions of different pH values.

Chapter 3

PDMS designed Microfluidic Chip

Chapter 3 introduces the capillary designed concept based a microfluidic chip, its fabrication and final replica mold shape for making PDMS based a microfluidic chip, advantages of using such PDMS-made microfluidic chip.

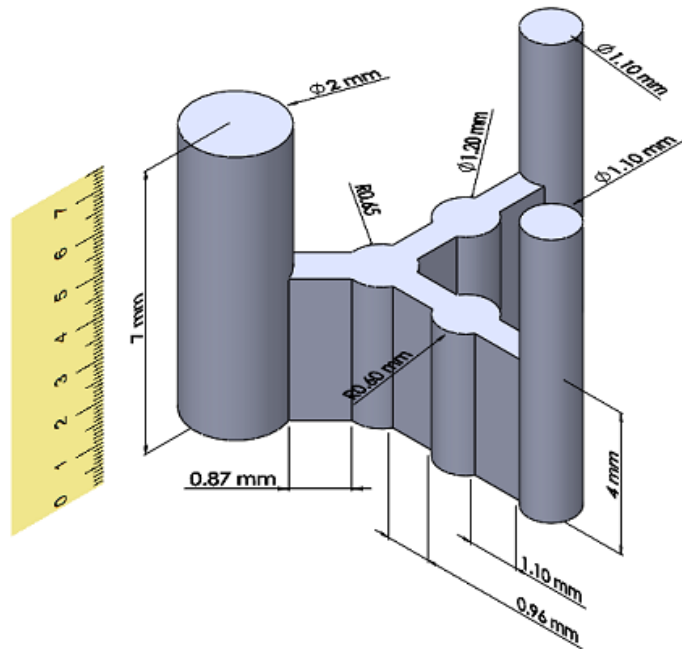


FIGURE 3.1: Different dimensions of micro flow channels' 3D lay out in Solid work.

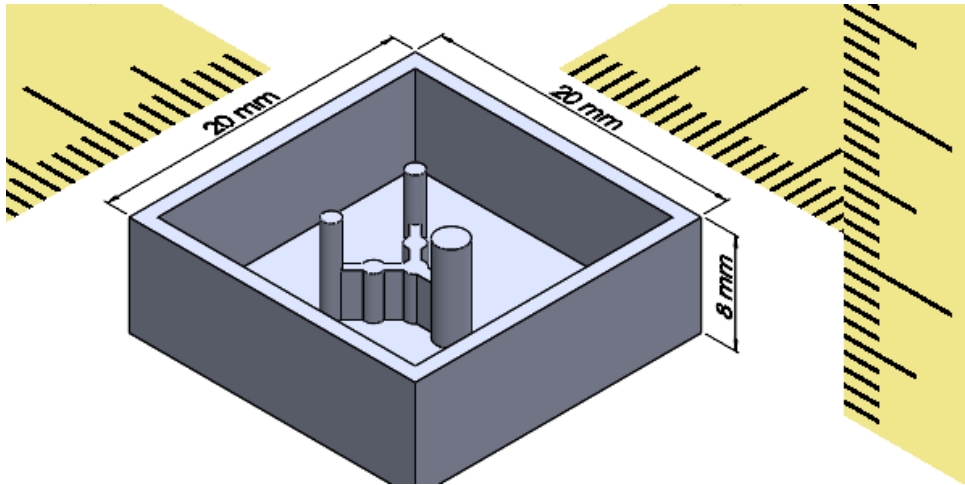


FIGURE 3.2: 3D-printed structure of the microfluidic chip with dimensions of $20\text{ mm} \times 20\text{ mm}$ scaling in Solid work

3.1 Preparation of PDMS

PDMS [Bor+18] is frequently used to fabricate micro total analysis systems [Cul+14; ZH19] and lab-on-a-chips [MT17]. One base and one curing agent named, a sylgard® 184 silicone elastomer base agent and a sylgard ®184 silicone elastomer curing agent as an adhesive were chosen to fabricate PDMS replica mold that are manufactured by Dow Corning (Midland, Maryland, USA). A PDMS-made microfluidic structure was developed followed by an irreversible assembly process using the above mentioned base and curing agents. Two inlet wells and one outlet well based (Fig. 3.1) a 3D structure of a microfluidic chip was drafted using a student version Solid work software, translated it into STL format (Fig. 3.2) and then printed the structure (Fig. 3.3) from the high definition 3D printer (Agilista-3100; serial no.: 96M14458) for this research work. PDMS sample made microfluidic chip was developed by cross-linking both the base and curing agents at a mass ratio of 10:1 [Ver+14; Ahm+21].

In the next step, for the fabrication of a replica mold of the 3D structure, the two cross-linked base and curing agents were poured into this structure of the dimensions of $20\text{ mm} \times 20\text{ mm}$ and height of 7 mm from the upper part of base surface (Fig 3.3 and Fig. 3.10). The poured solutions were then placed

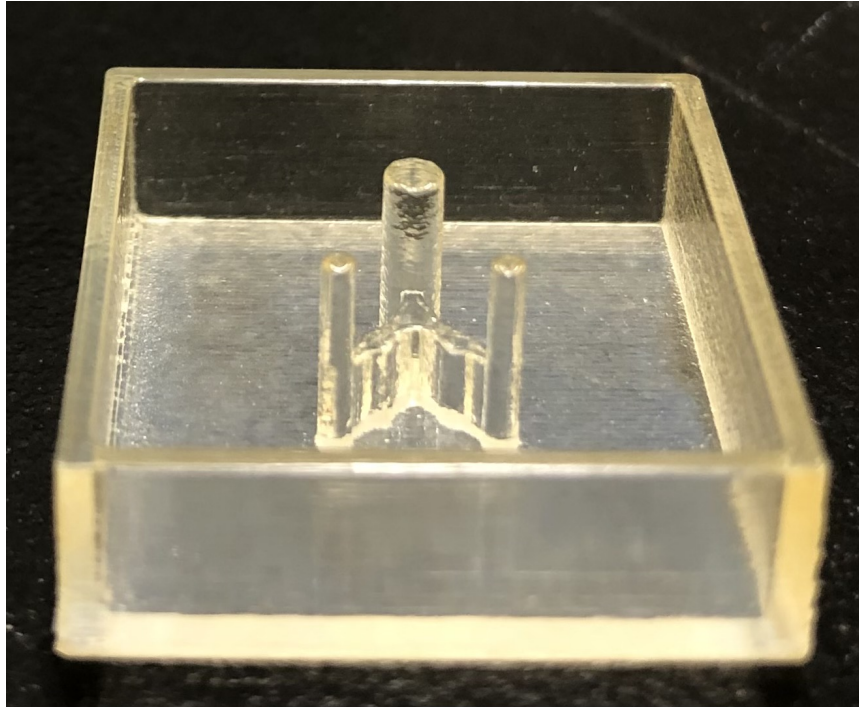


FIGURE 3.3: practical 3D printed structure for preparing replica of this structure

into an oven at a controlled temperature of 40°C for 24 h for the confirmation of sufficient hard shape of the replica mold (Fig. 3.4). The main part of central micro flow channels were designed at the height of 7 mm for each of two inlets and the only outlet from the upper part of base surface and at the height of 4 mm of internal micro flow channels from the top part of the base surface of the 3D printed structure (Fig.3.1). When the replica mold within the structure is hard enough, the replica mold was cut manually from the dimensions of 20 mm × 20 mm structure to the dimensions of 10 mm × 10 mm (Fig. 3.5). Thus, a PDMS made microfluidic chip was formed for doing the experiment. The bottom part of the microfluidic chip was attached with a Si: sapphire glass substrate to ensure the flow of fluids without any interruption or the leakage inside the micro flow channels of the microfluidic chip [Ahm+21].

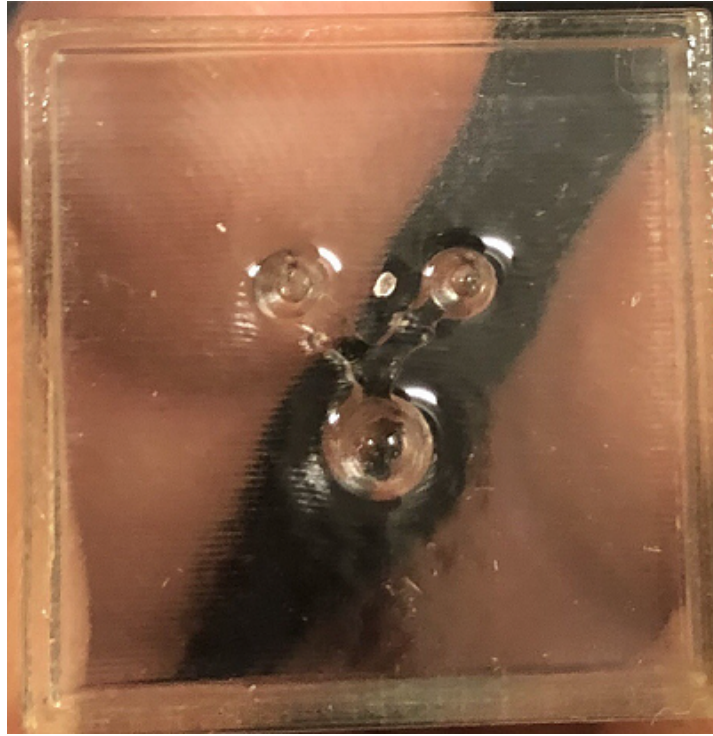


FIGURE 3.4: Hard replica mold within 3D printed structure

3.1.1 Top and bottom plates design to squeeze PDMS

It was difficult to ensure intensive flow of fluids through the micro flow channels without any upper external support to squeeze the PDMS-made microfluidic chip. Therefore, a similar top plate (Fig. 3.7) of 40 mm × 40 mm was designed, screwed and tilted mechanically with the bottom sensing plate (Fig. 3.6) by squeezing the microfluidic chip (Fig. 3.9) with the Si: sapphire glass substrate. As a result, without any risk of the leakage of the solutions outside the micro flow channels, the spontaneous flow of butter solutions was ensured. As a precautionary step, in order to avoid any chance of the leakage of the fluidic solutions outside the micro flow channels, the screwing and tilting should be balanced enough for the microfluidic chip during the experiment time [Ahm+21].

The whole procedure for the experimental microfluidic chip with such arrangement is shown in Fig. 3.9 below.

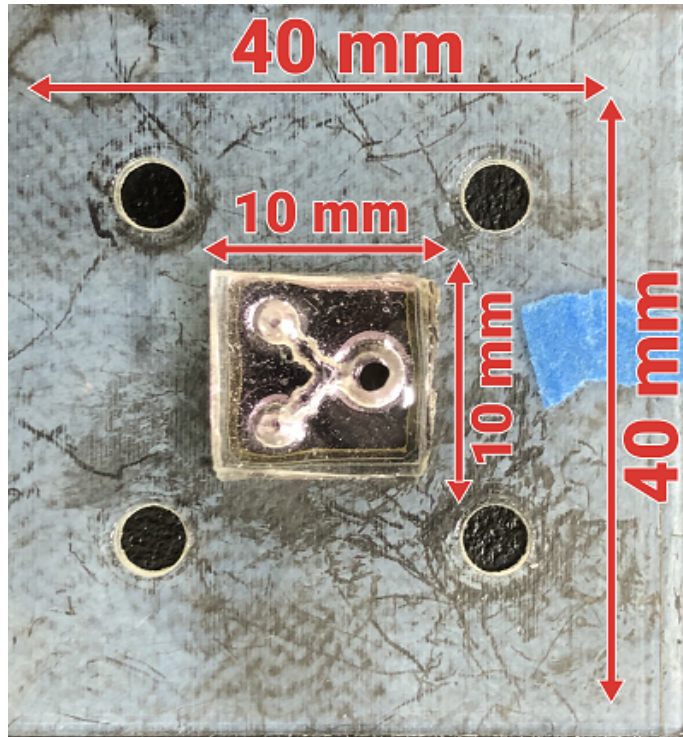


FIGURE 3.5: Manual cut microfluidic chip attached with Si:sapphire glass substrate (clipped with bottom 3D printed plate)

3.1.2 Cross-sectional view of designed micrfluidic chip and isometric view of central main structure of microfluidic chip

The top isometric view of the designed chip (Fig. 3.11), side cross sectional view (Fig. 3.10) and top close dimensional view (Fig. 3.8) were drawn in solid works software [SSW15; Mat13] to understand the design criteria.

3.1.3 Advantages and key features of PDMS

The primary advantages [Bor+18] of it over other substrate materials are the economic feature with low cost, easy and fast fabrication, high gas permeability and excellent optical transparency through the visible wavelengths into the near ultra-violet wavelengths and chemical inertness. Also, the interesting features of low shrinkage rate and the capability to replicate micro-scale environment make PDMS to suit nicely with soft lithography and 3D structure printing processes.

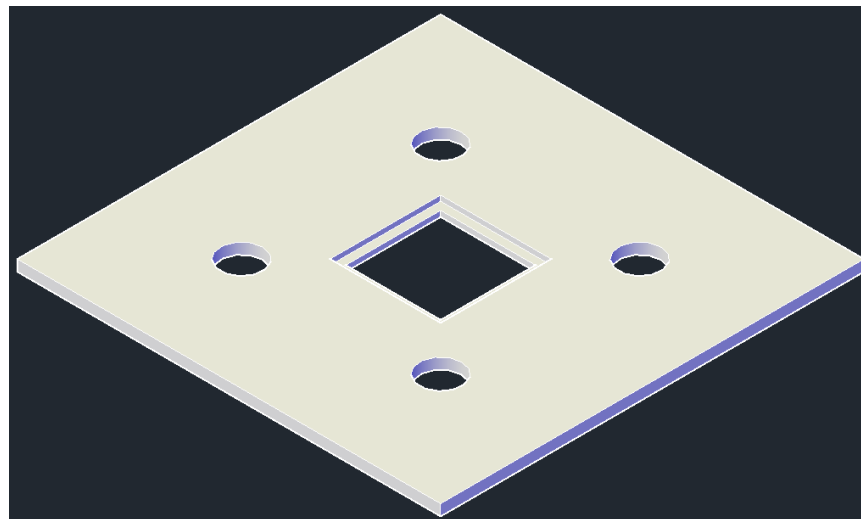


FIGURE 3.6: Bottom plate designed in CAD software (In the middle, Si:sapphire glass substrate of 10 mm × 10 mm was clipped and PDMS-made MC was attached with glass substrate

3.1.4 Summary

PDMS is so popular material used for the fabrication of microfluidic chip in the clean room and laboratories using different photolithographic process and 3D printing technique. Here in this dissertation, PDMS-made microfluidic chip was used efficiently to test chemical solutions for the control quality control of pH controlled foods.

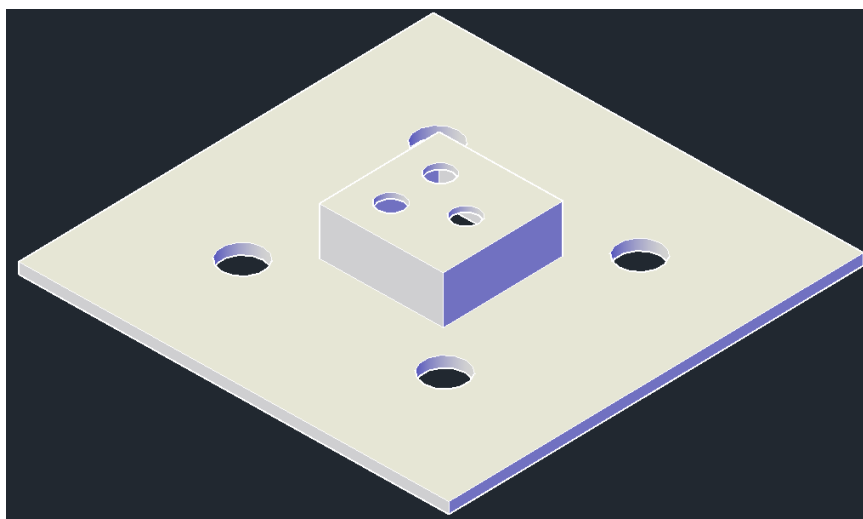


FIGURE 3.7: Top plate designed in CAD to squeeze the microfluidic chip with glass substrate and bottom sensing plate

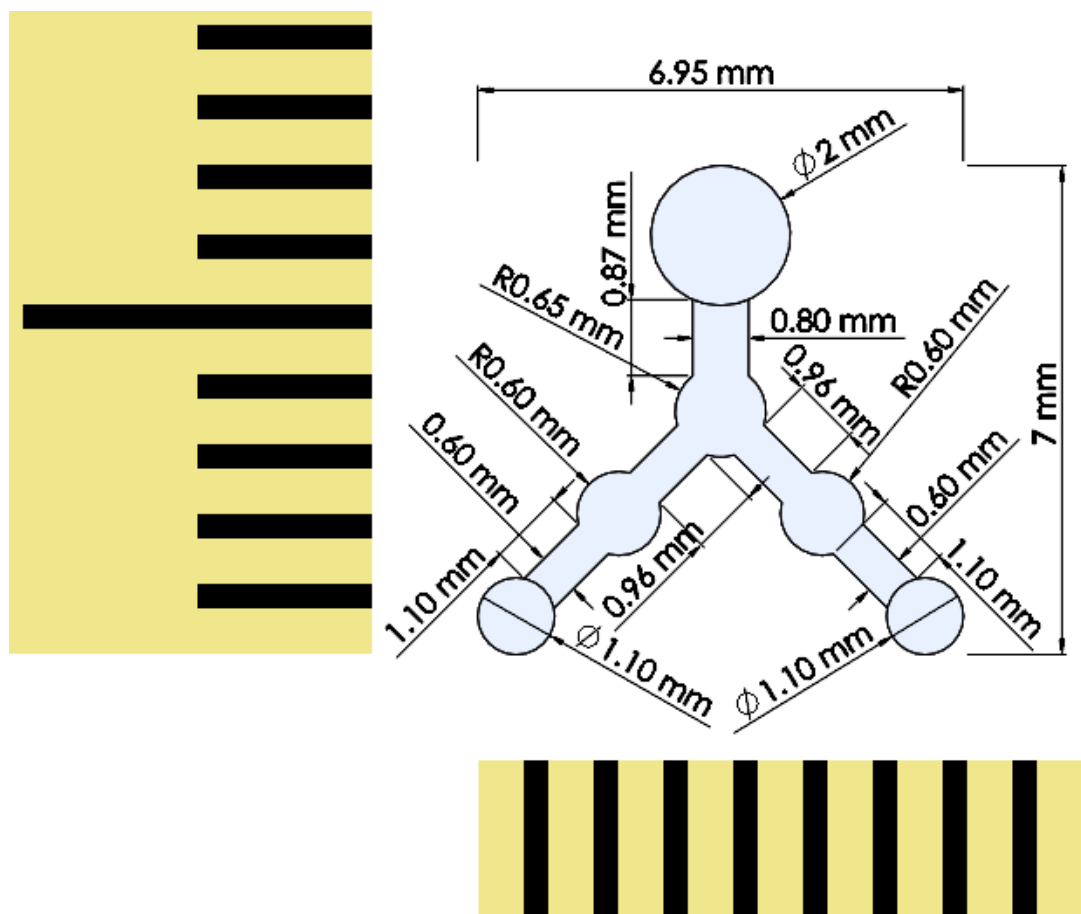


FIGURE 3.8: Top view of internal micro fluidic channels formation in Solid works using different internal designed dimensions

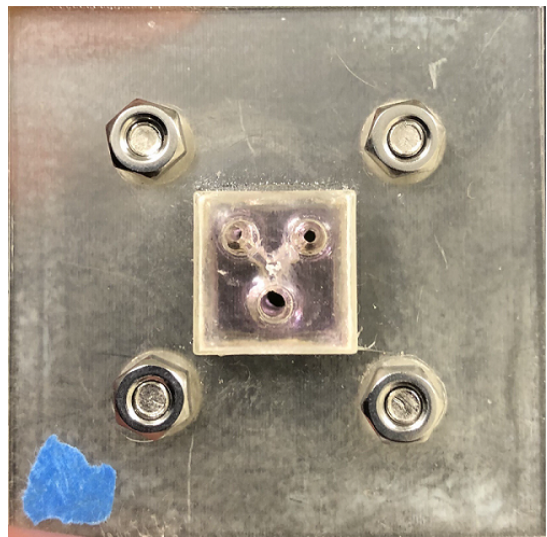


FIGURE 3.9: Microfluidic chip that attached with Si:sapphire glass substrate, screwed and tilted in a balanced way to squeeze it with top and bottom plate

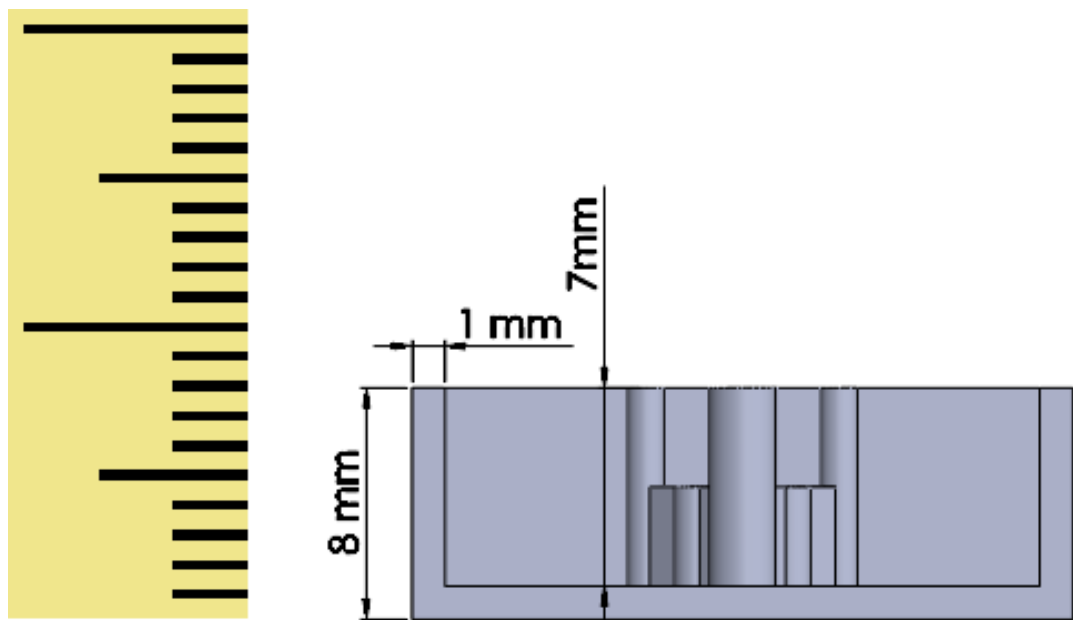


FIGURE 3.10: cross-sectional view of designed 3D structure

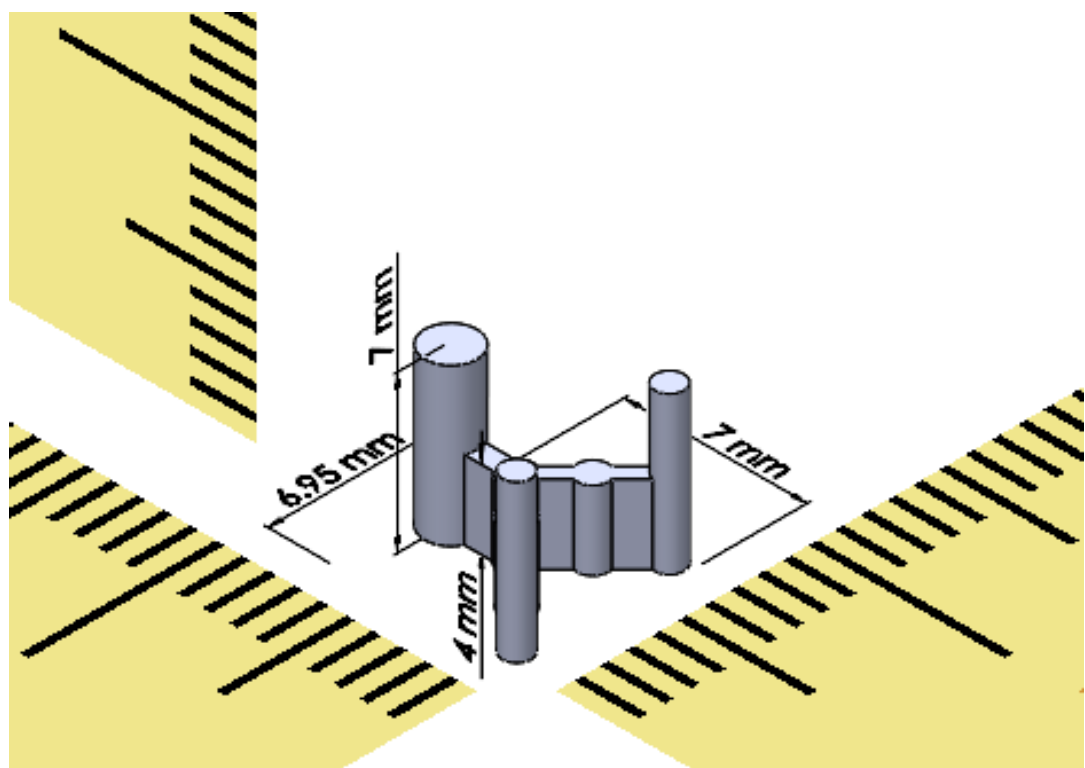


FIGURE 3.11: Scaling in solid work of main microfluidic chip's lay out along with micro flow channels

Chapter 4

Microfluidic Parameters Measurement, Calculation and Statistical Analysis

4.1 Introduction

Background and Motivation

Evaluation of microfluidic parameters for the analysis of the performance of a microfluidic chip is important because the clam and quiet nature of flow of fluids solutions can give the suitable micro-scale environment for the analysis of chemical and biological samples like pH controller liquid food samples, blood samples etc.

4.2 Mathematics

On the basis of nature of the geometry of the micro flow channels , the way it is combined the resistances of electrical circuit components, the similar way micro fluidic resistances (MFR) participate to calculate the total resistance of a microfluidic platform. According to the concept of the electrical circuit model,

to deduce fluid flow rate, MFR values and given pressure drop applied to a microfluidic chip followed by the Hagen- Poiseuille's equation [PPUn a] is used:

$$\Delta P_n = Q_n R_f \quad (4.1)$$

where R_f is the MFR of micro flow channels, Q_n is the volumetric different fluid flow rates and ΔP_n is different pressure drops across the micro flow channels correspond to different fluid flow rates respectively. $n = 1, 2, 3, \dots, N$. In case of laminar nature of an isothermal, incompressible and isotropic Newtonian fluid flow through a tube or cylindrical shaped inlets and one outlet with a circular cross section and no-slip boundary conditions on sidewalls of microfluidic structure, the MFR can be modeled mathematically [GGBY16] below:

$$R_{Tubing} = R_{Circular/Cylinder} = \frac{128\mu L}{\pi d^4} \quad (4.2)$$

where μ = viscosity of a fluid, L = length of the given tube or cylindrical shaped well, d = diameter of the given tube or cylindrical shaped well. $\frac{1}{d^4}$ term signifies that even a small change in d , there will be a vast change in values of fluidic resistances. For the rectangular cross section, fluid flow rate, Q can be formulized in terms of pressure drop ΔP over the micro flow channels' length, L according to equation 4.1 and can be deduced as:

$$Q = \Delta P \frac{w_1 h^3}{12\mu L} \quad (4.3)$$

The pressure drop ΔP can be expressed to show a relation in between hydrodynamic resistance [GGBY16; BL17] in the channel, R_H , also called chip resistance, R_{chip} and the FFR similar to the voltage drops in electrical current.

$$\Delta P = QR_H = Q \frac{12\mu L}{w_1 h^3} \quad (4.4)$$

where

$$R_H = R_{chip} = \frac{12\mu L}{w_1 h^3} \quad (4.5)$$

w_1 is in between width and height of rectangular channels of smaller dimension and h is the height of larger dimension. Equation 4.5 is to calculate the hydrodynamic or chip resistance . The continuity equation [PPUn b] is,

$$Q = A_1 \bar{v} \quad (4.6)$$

where A_1 = area of either a circular or a rectangular path and \bar{v} is the average velocity of a given fluid. Area of inlets/outlet, $A_1 = 2\pi r(r+h)$ where r =radius of cylindrical shaped inlets/outlet and h =height of them. Reynolds number R_e is a dimensionless number to measure a fluid in motion qualitatively that evaluates the ratio of convective forces to viscous forces. It is expressed as:

$$R_e = \rho D_{hh} \frac{\bar{v}}{\mu} \quad (4.7)$$

where \bar{v} is the average fluid velocity and D_{hh} is the characteristic length of a fluid. $R_e \leq 2300$ means the flow is laminar and. $R_e > 2300$ means the flow is turbulent [PPUn a].

4.3 Calculation of Microfluidic Resistances of Microfluidic Chip

From the experiment in the laboratory, it was measured the viscosities of pH=4 and 10 buffer solutions of 0.5 mPa·s and 0.59 mPa·s respectively. The viscosity of pH=4 and 10 mixed solution is 0.58 mPa·s. The given length of each of two syringes connected two tubes was 2 m length and 2 mm diameter. THe designed microfluidic chip of two inlet wells and one outlet well based micro flow channels consisted of the intermediate wells, a common junction well (CJW) and

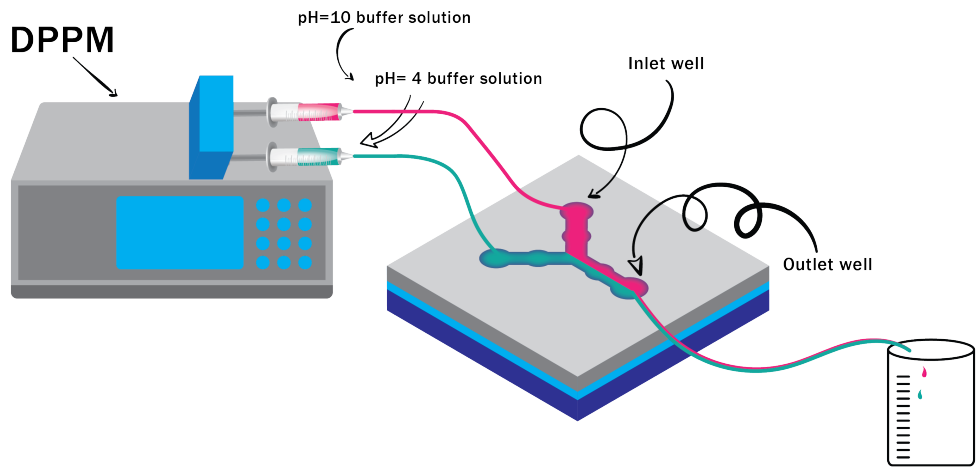


FIGURE 4.1: Digital pressure machine (DPM) controlled fluids flow through a capillary design based microfluidic chip

rectangular paths which was drawn in Fig. 4.4.

The mixed accumulated buffer solutions into the common junction well were flushed out through the outlet well into a beaker using a tube of 1 m length and diameter of 2 mm. The height of each of two inlet wells and one outlet well were 7 mm from the fabricated base surface of the MC structure and the height of micro flow channels was 4 mm from that of the base surface. Therefore, using all of the above fluid flow parameters for different dimensions of microfluidic chip, we calculated tubing resistances [GGBY16] for the syringes connected tubes, chip resistances [BL17] for the rectangular paths and cylindrical resistances [GGBY16] for the circular (Fig. 3.1) shaped cylindrical fluid flow paths with the other hydrodynamic properties of the injected pH=4 and 10 buffer solutions using equations 4.2 and 4.5 that sketched in Fig. 3.1. In the Fig. 4.2, from the sides of pH 4 and 10 buffer solutions, if we move towards the final common path of these mixed two solutions, we can find that the values of all types of microfluidic resistances are decreasing gradually. It means that from the injected flow paths of both pH 4 and 10 buffer solutions, the fluid flow rates are increasing according to the equation 4.1 at the final destination of the flushed out of the mixed two buffer solutions via a beaker.

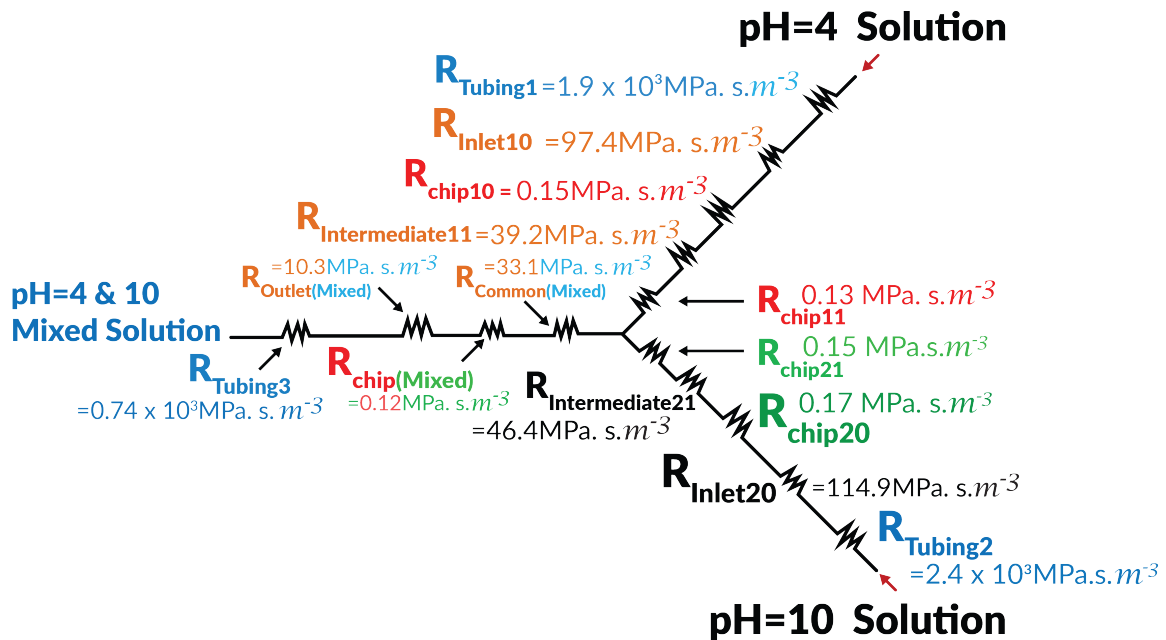


FIGURE 4.2: Internal rectangular, cylindircal resistances calculation of the desinged microfluidic chip

During the design of the microfluidic chip, the diameter of the outlet well and the dimensions of all different patterned common paths towards the outlet well were made larger in comparison with the diameters of each of two inlets and other different dimensions with different patterned (rectangular paths, circular shaped cylindrical paths) fluid flow paths. Because after the mixture of two fluids, heat transfer, temperature change and other internal parameters inside the micro flow channels might affect the nature of mixed fluids widely. For pH=4 solution's injected fluid flow path, if the number of MFR arranged in series, an equivalent single microfluidic resistance has a hydraulic resistance equal to the sum of four hydraulic resistances [Oh+12].

$$R_{1eq.} = R_{inlet10} + R_{chip10} + R_{intermediate11} + R_{chip11} \quad (4.8)$$

$$R_{1eq.} = 169.85 \text{ MPa.s.m}^{-3} \quad (4.9)$$

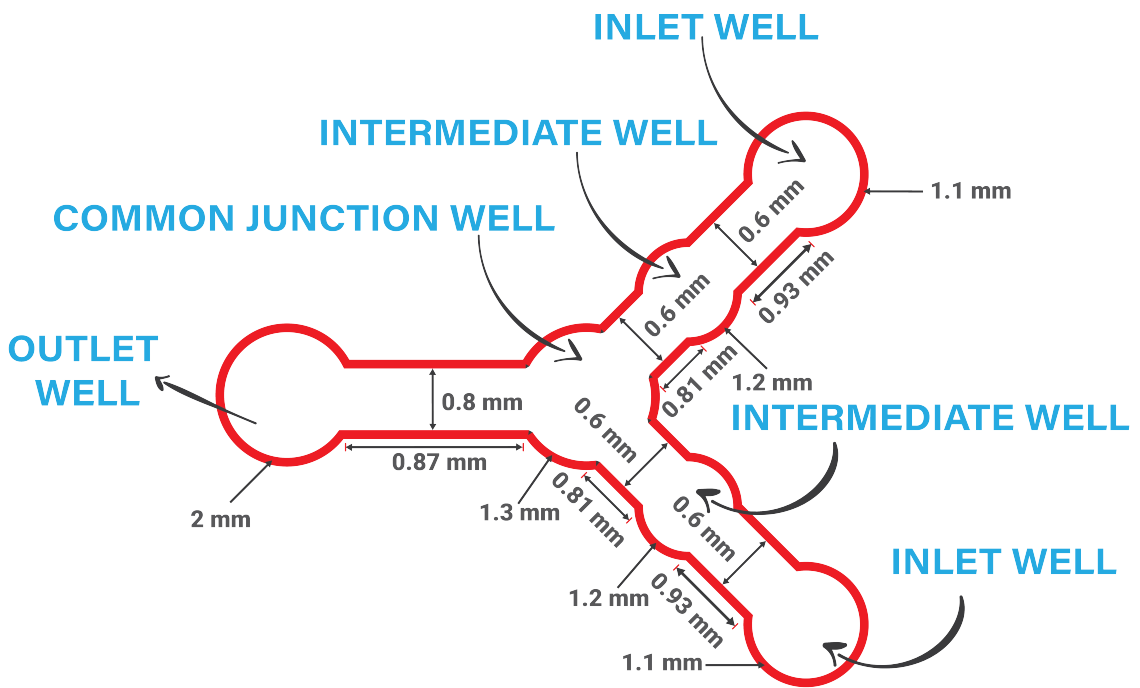


FIGURE 4.3: Different internal dimensional microfluidic wells of the microfluidic chip

Similarly, for pH=10 Solution, the injected Fluid Flow Path (FFP),

$$R_{2eq.} = R_{inlet20} + R_{chip20} + R_{intermediate21} + R_{chip21} \quad (4.10)$$

$$R_{2eq.} = 161.62 \text{ MPa.s.m}^{-3} \quad (4.11)$$

And, for Mixed common FFP,

$$R_{3eq.} = R_{com.mix} + R_{chip_{mix}} + R_{out.mix} \quad (4.12)$$

$$R_{3eq.} = 43.52 \text{ MPa.s.m}^{-3} \quad (4.13)$$

As an external pressure source driven MC, we denoted our used syringe pump conveying fluids flow through two tubes as independent constant fluid flow

sources Q_{S_1}, Q_{S_2} . Practically, our MC were connected with digital pressure machine via syringe-connected tubes where two inlets and one outlet normally opened at atmospheric pressure to flush out the mixture of two pH BS. From the electrical circuit analogy [Oh+12] compared with the microfluidic network analogy, the outlet is regarded as a ground as it was opened at the atmospheric pressure. The equivalent MFR of entire MC was drawn in Fig. 4.4. It was

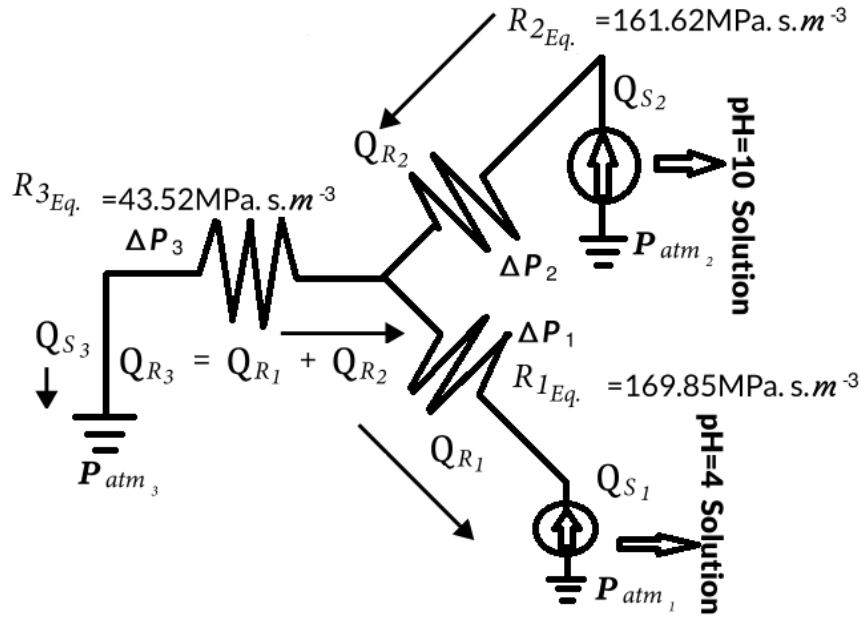


FIGURE 4.4: Equivalent MFR calculation to find out resultant fluid flow rate and pressure drop of entire microfluidic chip

found out R_e at outlet well of microfluidic chip by calculating average velocity from the experimental measured values of different fluid flow rates. For outlet well, mixed solutions' density is 0.9901 g/mL. Average velocity at outlet well according to the experimental measured different fluid flow rates is calculated below:

$$v = \frac{(0.031 + 0.057 + 0.09 + 0.14 + 0.3 + 0.15 + 0.39 + 0.481)}{7} \quad (4.14)$$

$$v = 0.21 \text{ ms}^{-1} \quad (4.15)$$

Therefore, from (7), we got $R_e = 2.51$.

TABLE 4.1: Pressure drops through pH=4 inlet well for the certain ranges of set values of fluid flow rates from DPM

Inlet Flow rate, $Q_n, mL/min$	$\Delta P_1, Pa$	$\Delta P_2, Pa$	$\Delta P_3, Pa$	$\Delta P_4, Pa$	$\Delta P_5, Pa$	Average Pressure drop, Pa
0.03 to 0.07	0.049	0.065	0.081	0.097	0.114	0.0812
0.09 to 0.13	0.146	0.162	0.179	0.195	0.211	0.1786
0.14 to 0.18	0.227	0.244	0.26	0.276	0.292	0.2598
0.23 to 0.27	0.373	0.39	0.406	0.422	0.438	0.4058
0.38 to 0.42	0.617	0.633	0.649	0.666	0.682	0.6494
0.58 to 0.62	0.942	0.958	0.974	0.99	1.007	0.9742
0.78 to 0.82	1.266	1.283	1.299	1.315	1.331	1.2988
0.97 to 1.01	1.575	1.591	1.607	1.624	1.64	1.6074

4.4 Pressure Drop Measurement and Velocity Profile Estimation from Fluid Dynamics

During the experiment, the digital pressure machine was set at different fluid flow rates by pumping two syringe-connected tubes automatically to allow the flow of pH=4 and 10 buffer solutions through the designed microfluidic chip. Different pressure drops corresponding to different five “set values” of fluid flow rates from digital pressure machine were calculated for two inlet wells from equation 4.1 by putting the values of cylindrical resistances, $R_{inlet10}$ and $R_{inlet20}$ of two inlet wells from Fig. 4.2. Then, by choosing certain intervals (viz. 0.3 to 07 mL/min, 0.09 to 0.13 mL/min etc.) for different fluid flow rates, the average pressure drop was calculated (Table 4.1 and Table 4.2) for each of fluid flow rate’s interval at two inlet wells and data were plotted that increased monotonically (Fig.4.5) with the increased fluid flow rates in case of two pH buffer solutions.

In Fig. 4.6, with the increased values of fluid flow rate through the microfluidic chip, the average pressure drop increased linearly to satisfy the equation 4.1 of Hagen-Poiseuille’s law of fluid dynamics. During the experimental measurement, each reading of pressure drop was taken five times repeatedly with

TABLE 4.2: Average Pressure drop through pH=10 inlet well for the certain ranges of set values of fluid flow rates from DPM

Inlet Flow rate, $Q_n, mL/min$	$\Delta P_1, Pa$	$\Delta P_2, Pa$	$\Delta P_3, Pa$	$\Delta P_4, Pa$	$\Delta P_5, Pa$	Average Pressure drop, Pa
0.03 to 0.07	0.057	0.077	0.096	0.115	0.134	0.0958
0.09 to 0.13	0.172	0.192	0.211	0.23	0.245	0.21
0.14 to 0.18	0.268	0.287	0.306	0.326	0.345	0.3064
0.23 to 0.27	0.441	0.46	0.48	0.5	0.517	0.4796
0.38 to 0.42	0.728	0.747	0.766	0.785	0.804	0.766
0.58 to 0.62	1.111	1.13	1.149	1.168	1.188	1.1492
0.78 to 0.82	1.494	1.513	1.532	1.551	1.571	1.5322
0.97 to 1.01	1.896	1.915	1.935	1.877	1.858	1.8962

TABLE 4.3: Average pressure drop through outlet well from the experimental measured fluid flow rates

In each Inlet, $Q_{in}, mL/min$	Outlet Flow rate, $Q_0, mL/min$	$\Delta P_1, Pa$	$\Delta P_2, Pa$	$\Delta P_3, Pa$	$\Delta P_4, Pa$	$\Delta P_5, Pa$	Average Pressure drop, Pa
0.07	0.093	0.0159	0.0158	0.0161	0.162	0.016	0.016
0.1	0.17	0.029	0.031	0.03	0.028	0.28	0.0796
0.15	0.27	0.047	0.046	0.047	0.047	0.045	0.0464
0.25	0.41	0.07	0.07	0.073	0.076	0.071	0.072
0.4	0.59	0.102	0.103	0.1	0.101	0.1	0.1012
0.6	0.9	0.151	0.152	0.16	0.155	0.156	0.1548
0.8	1.16	0.2	0.201	0.2	0.202	0.2	0.2006
1	1.45	0.25	0.25	0.252	0.25	0.251	0.2506

respect to the same fluid flow rate using trial and error method. Then, each average pressure drop data was calculated with respect to each fluid flow rate and found out the range of standard deviation for each average pressure drop value. From the graph, all average pressure drop data followed linear nature except 0.15 mL/min data that was deviated from the normal criteria because of error in trial and error method during the measurement time. The microfluidic resistance $R_{outletmixed}$ at the outlet well was taken from the calculated resistance values of Fig. 4.2.

The average pressure drop (refer to Table 4.1 and Table 4.2) in each interval

TABLE 4.4: Average velocity through outlet well from the experimental measured fluid flow rates

Outlet Flow rate, $Q_0, mL/min$	$v_1, mm/s$	$v_2, mm/s$	$v_3, mm/s$	$v_4, mm/s$	$v_5, mm/s$	$v_{Avg.}, mm/s$
0.093	0.031	0.03	0.031	0.031	0.03	0.0306
0.17	0.056	0.059	0.058	0.055	0.055	0.0566
0.27	0.091	0.088	0.091	0.09	0.087	0.0894
0.41	0.134	0.134	0.14	0.15	0.14	0.1396
0.59	0.292	0.3	0.305	0.3	0.302	0.2998
0.9	0.151	0.152	0.16	0.155	0.156	0.1548
1.16	0.39	0.39	0.38	0.39	0.39	0.388
1.45	0.474	0.48	0.49	0.481	0.484	0.4818

TABLE 4.5: Average velocity measurement through inlet wells using "set values" of the fluid flow rates of DPM

Inlets Flow rate, $Q_{in}, mL/min$	$v_1, mm/s$	$v_2, mm/s$	$v_3, mm/s$	$v_4, mm/s$	$v_5, mm/s$	$v_{Avg.}, mm/s$
0.03 to 0.07	0.019	0.026	0.032	0.038	0.045	0.032
0.09 to 0.13	0.057	0.064	0.07	0.077	0.083	0.0702
0.14 to 0.18	0.089	0.096	0.102	0.109	0.115	0.1022
0.23 to 0.27	0.153	0.255	0.166	0.172	0.147	0.1596
0.38 to 0.42	0.243	0.377	0.249	0.262	0.268	0.2554
0.58 to 0.62	0.37	0.152	0.383	0.39	0.4	0.384
0.78 to 0.82	0.498	0.505	0.511	0.517	0.523	0.5108
0.97 to 1.01	0.62	0.626	0.632	0.639	0.645	0.6324

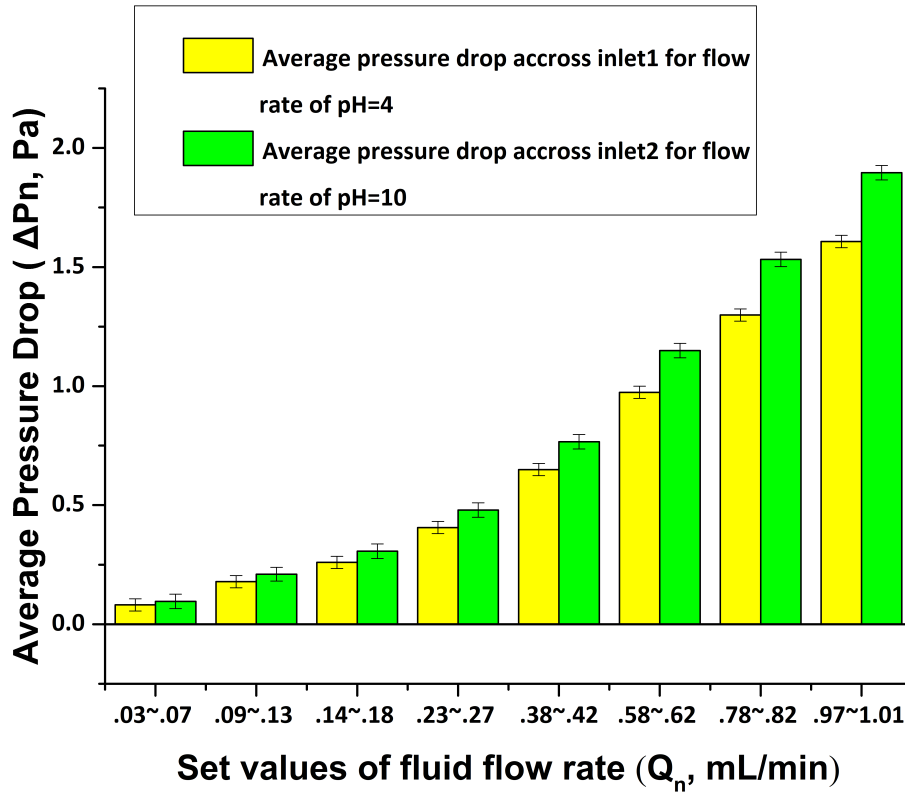


FIGURE 4.5: Estimation of average pressure drop across the points of two inlet wells using set values of fluid flow rates.

of fluid flow rate (Fig. 4.5) is higher than the average pressure drop (Table 4.3) in each case at the outlet well of Fig. 4.6. Because syringe-connected tubes experienced huge pressure drop as the air did not be able to fully escape from inside the syringes in reality. To push into the plungers of syringes automatically by digital pressure machine, the air inside the plungers of two syringes were compressed into smaller volume that created much high pressure inside the two syringes. As a consequence, this high pressure automatically applied to the tubes connected with the syringes that affected the effective diameters of flexible structure of two tubes instantaneously to handle the high Pressure drop inside the tubes. Therefore, these two syringe-connected tubes were connected with two inlet wells that created overall higher impact on the pressure drop inside the two inlet wells than that of a tube connected outlet well. There is also another important reason of such type of higher pressure drop across

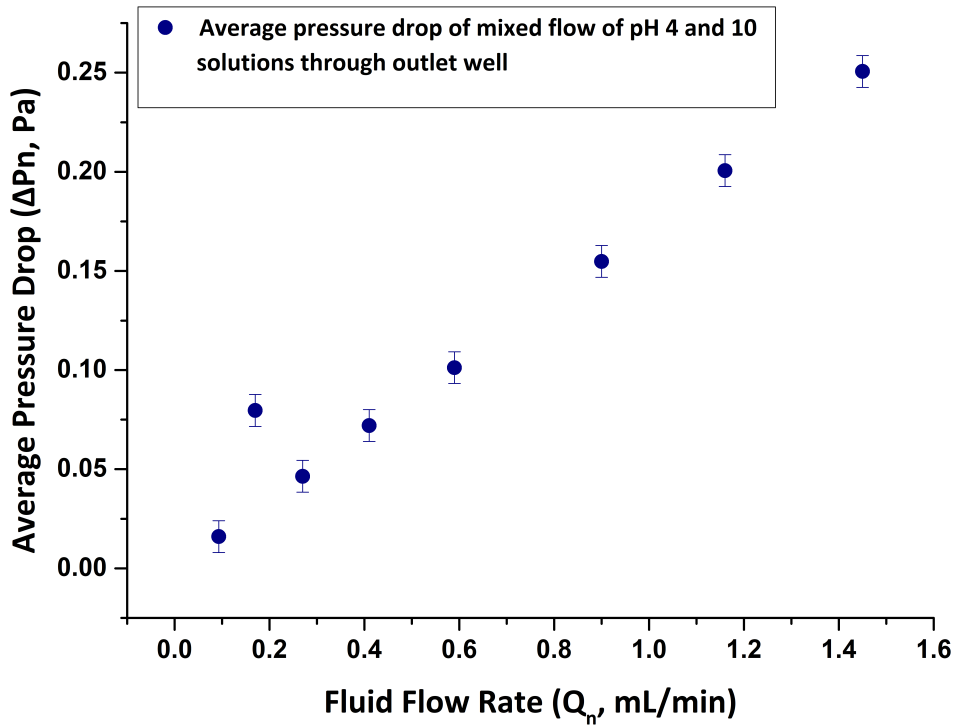


FIGURE 4.6: Quantitative data analysis of average pressure drop across the point of only outlet well using experimental measured values of fluid flow rates.

the two inlet wells. The diameter of each of cylindrical shaped two inlet wells designed (1.1 mm each) was lower than the diameter of outlet well (2 mm). As a result, the pressure drop across two inlet wells experienced higher pressure drop 4.5 compared with that of outlet well 4.6, according to the equation 4.1 where pressure drop is proportional to the fluid flow rate.

In Fig. 4.7, the average velocity at the outlet well was estimated by taking five readings (refer to Table 4.4) of measured value of same fluid flow rate at the outlet well. For doing this measurement, mixed pH 4 and 10 buffer solutions were flushed out automatically into a beaker through a tube-connected with only outlet well of the microfluidic chip. Then, the volume of taken-out mixed fluids calculated from the total occupied volume of the beaker in mL for the certain programmed total measurement time. As a result, each fluid flow rate

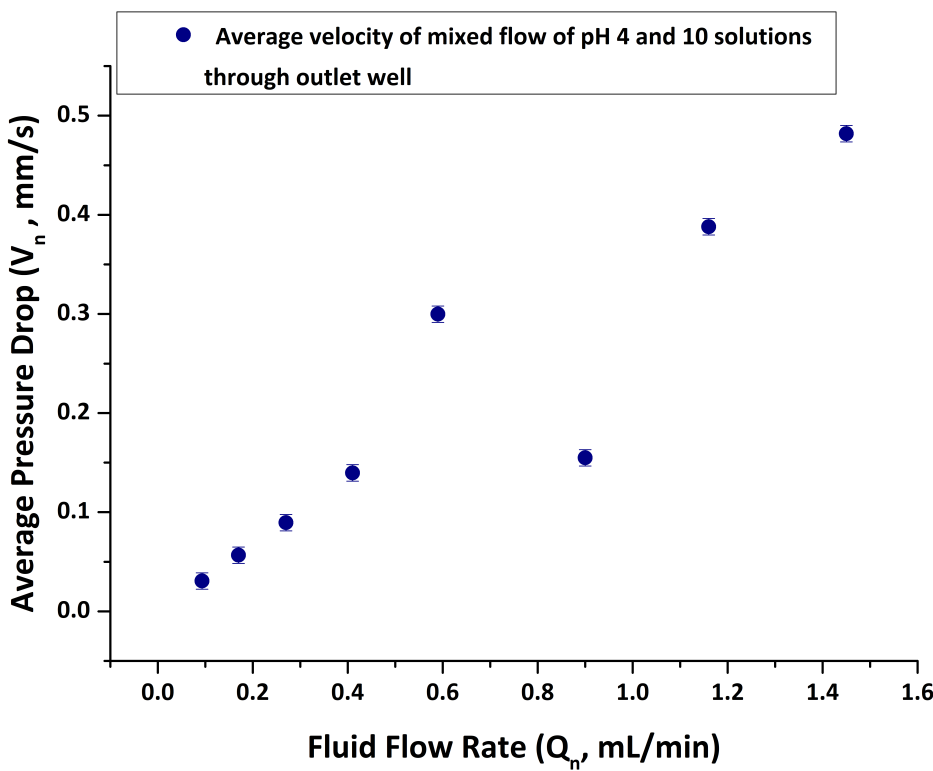


FIGURE 4.7: Statistical data analysis of average velocity versus fluid flow rate through the outlet well

was calculated. From such five readings of each of fluid flow rate, five readings of velocity was calculated in each case and using equation 4.6, average velocity was calculated. The curve was plotted to find the different average velocities at the outlet well for different fluid flow rates. The curve shows linear nature of average increased velocity with respect to different fluid flow rates except the fluid flow rates at 0.6 and 0.7 mL/min because of the error in trial and error method during the experimental measurement time.

In the Fig.4.8, using equation 4.6, for different "set values" of fluid flow rates from digital pressure machine, average values of certain interval of fluid flow rates (viz. $0.3\text{mL}/\text{min}$ to $0.07\text{mL}/\text{min}$, $0.09\text{mL}/\text{min}$ to $0.13\text{mL}/\text{min}$ etc.) were calculated (refer to Table 4.5) and plotted that increased monotonically the increased intervals of fluid flow rates. During the design process, the diameter of each inlet was designed at the same value of 1.1 mm. As a result, using

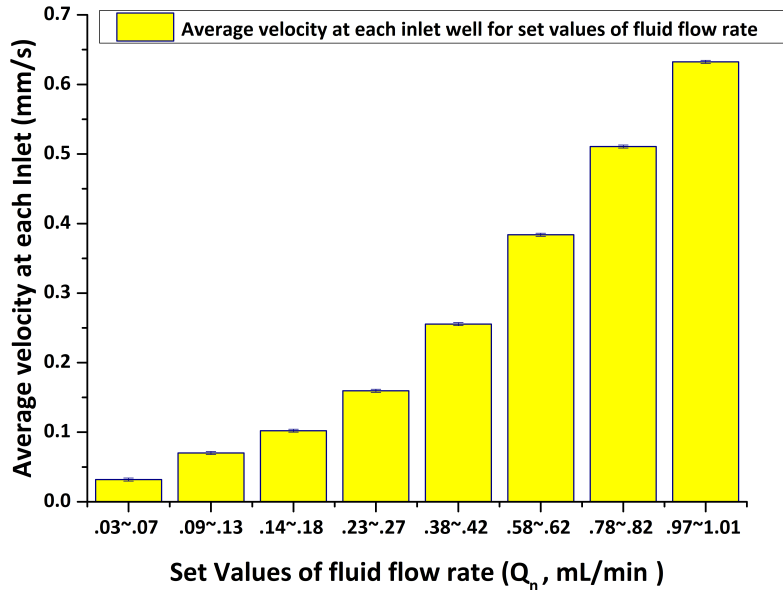


FIGURE 4.8: Statistical data analysis of average velocity versus fluid flow rate through the two inlet wells of same designed diameter in dimension

equation 4.6, same area was calculated in each case to get a gross idea of velocity profiles in each of two inlet wells of the microfluidic chip. Compared to the Fig. 4.7, average velocity is higher at the two inlet wells of Fig. 4.8 because of the diameter of outlet is larger (2 mm) than each of two inlet wells that tend to make the lower average velocity experienced by the only outlet well according to equation 4.6.

4.5 Summary

The internal microfluidic parameters of the designed microfluidic chip were statistically plotted, analyzed and evaluated. At the beginning, the microfluidic resistances were calculated for the internal different patterned micro flow channels. The outcome of this experimental results is used for the emphasis with the simulation results.

Chapter 5

Simulation to Emphasize the Experimental Result

5.1 Introduction

Use of ANSYS Fluent software for computational fluid dynamics (CFD) simulation [SLL14] is specifically useful in case of the analysis, study of the behaviors of microfluidic flow that ranges from fundamental research to design of devices [B81], [HES13],[Kim+08]. This computational method shows its merits, including the design of robust devices and its capability to simulate the complex and coupled physics swiftly at very low cost[Gre+09]. A lot of fluid mechanics researchers used CFD simulator for studying the mechanism of hydrodynamics behavior of fluids and cell mechanical environments [CWL06], [YA12], [Liu+13], [Sun+13], [Xu+13]. The numerical simulation of internal flow of biological and chemical solutions through the microfluidic chip is necessary to compare with the experimental data as the performance of the microfluidic chip can be evaluated in terms of the behavior of the microfluidic parameters with the simulated and experimental data of the real world.

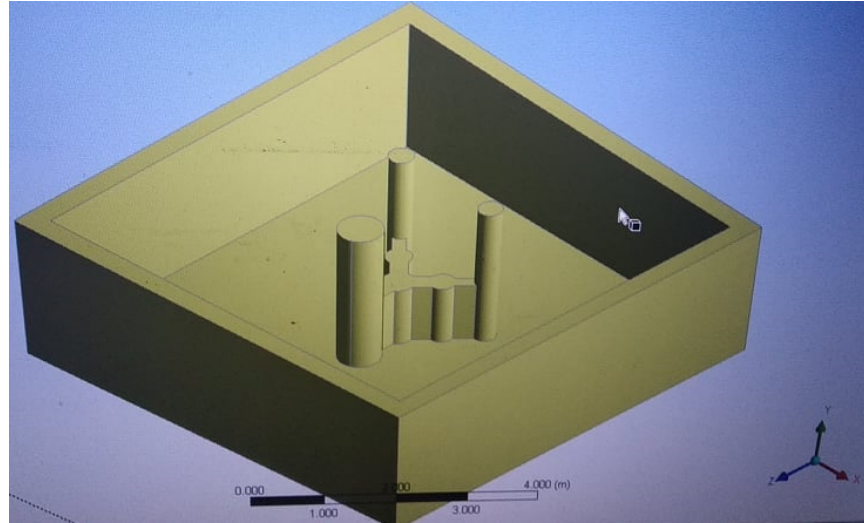


FIGURE 5.1: Exact dimensional 3D structure formed in ANSYS simulator to run the program with different microfluidic parameters of fluid dynamics

5.2 Simulation Algorithm

Physical Model and CAD Modelling

During the experiment, flow of two different pH buffer solutions have been realized through the micro flow channels through the microfluidic chip. The geometric structure narrated already in the chapter 4 with the reference of Fig. 3.1.

The flow of internal chemical buffer solutions through the channels were numerically solved with ANSYS academic version of Fluent workbench [Flu+11] when the experiment was performed with the designed microfluidic chip. The solid works model was implemented in the design modeler with suitable geometric structure (Fig.5.1) exactly same as the dimensions of the fabrication of the micro flow channels of the microfluidic chip. For selecting better convergence criteria and reducing the computational cost, the model was precisely reduced to the axial symmetry of the domain into a planar two-dimensional section. The viscosities and densities of different pH buffer solutions were considered with other properties of water listed in Table 5.1 using numerical model. Using the

TABLE 5.1: Measured Different Fluidic Parameters Given As Input Data And Calculated Input, Output Data.

pH Buffer Solutions	Viscosity, $mPas^{-3}$	Density, (g/mL)	Reynd Number	Microfluidic Resistances, $MPas^{-3}$
pH=4, Inlet 1	0.5	0.982	3.71	1.9×10^3
pH=10, Inlet 2	0.59	0.992	3.18	2.4×10^3
Mixed pH 4 and 10, Outlet	0.58	0.99	2.51	10.3

experimental measured data, all microfluidic parameters were calculated.

Governing equations

During the experiment, the mixing and others properties of fluid dynamics were examined in the outlet section. In order to track between the interface of mixing pH solutions, multi-phase volume of fluid (VOF) [BGP08; HN81; Eri05b; Kat19] with two Eulerian phases had been considered. For the dynamic behavior of these different pH fluids' coalescence in stagnant environment, the continuity, energy and momentum governing equations [KCD16a] of fluid dynamics were activated in this numerical approach too. They were approached by following the Euler form.

equation of continuity:

$$\nabla \cdot v = 0 \quad (5.1)$$

$$\frac{\partial \alpha_1}{\partial t} + v \cdot \nabla \alpha_1 = 0 \quad (5.2)$$

equation of momentum:

$$\frac{\partial(\rho v)}{\partial t} + \nabla \cdot (\rho v v) = -\nabla p_{st} + \nabla \cdot [\mu(\nabla v + \nabla v^T)] + F_{css} \quad (5.3)$$

equation of energy:

$$\frac{\partial(\rho h)}{\partial t} + \rho v \cdot \nabla h = \nabla(\lambda \nabla T) \quad (5.4)$$

where v is the fluid velocity (m/s) , ρ is the fluid density (kg/m^3), p_{st} is the pressure (Pa), μ is the dynamic viscosity ($\rho Pa.s$), α_1 is the thermal diffusivity, T is the temperature, λ thermal conductivity, h is the internal energy and F_{css} is the surface tension.

For the 2 phases, in each of control volume, density, viscosity, thermal conductivity are given by the following equations.

$$\rho = \alpha_1 \rho_w + (1 - \alpha_1) \rho_0 \quad (5.5)$$

$$\mu = \alpha_1 \mu_w + (1 - \alpha_1) \mu_0 \quad (5.6)$$

$$\lambda = \alpha_1 \lambda_w + (1 - \alpha_1) \lambda_0 \quad (5.7)$$

In general form, for a system of n-phase, all other properties in the volume-fraction-averaged will take on the following form:

$$x = \sum \alpha_q x_q \quad (5.8)$$

The VOF model will treat the energy, E_e , and the temperature, T , as mass-averaged variables:

$$E_e = \frac{\sum_{q=1}^n \alpha_q \rho_q E_q}{\sum_{q=1}^n \alpha_q \rho_q} \quad (5.9)$$

where E_q for each phase is on the basis of the specific heat of that phase and the shared temperature. In this model, continuum surface force (CSF) model

TABLE 5.2: Validation Of Experimental And Simulation Based Fluidic Parameters.

$Q_I, mL/min$	$Q_O, mL/min$	pH4, ΔP_{I_1}	pH10, $\Delta P_{I_2}, Pa$	$\Delta P_{O_{Exp.}}^*$	$\Delta P_{O_{Sim.}} Pa$	$E., \Delta P_{O_{Sim.}} (\%)$
0.07	0.093	0.0812	0.0958	0.0012*	0.001	16.67
0.1	0.17	0.1786	0.21	0.0796	0.054	32.16
0.15	0.27	0.2598	0.3064	0.026*	0.017	34.62
0.25	0.41	0.4058	0.4796	0.045*	0.031	31.11
0.4	0.59	0.6494	0.766	0.1012	0.086	15.02
0.6	0.9	0.9742	1.1492	0.087*	0.091	-4.6
0.8	1.16	1.2988	1.5322	0.1106*	0.094	15.01
1	1.45	1.6074	1.8962	0.1606*	0.114	29.02

Values of asterik sign (*) indicate the application of regression method to select the nearest values compared with the simulation results to minimize the percentages of error,E.

[DKC15] was used to calculate surface tension force with non-conservative formulation.

For time-dependent VOF calculation, all governing equations narrated above, were solved using an explicit time-matching scheme. ANSYS Fluent automatically refined the time step for the integration of the volume of fractions' equations. However, it was influenced this time step calculation by modifying the "Courant number". Anyone can choose to update the volume fraction once for each time step, or once for each iteration within each time step. For the simulation purpose, very small time step was considered in our process and $1e^{-3}$ converging criteria was taken as the residual for all the equations. All the notations of above equations denote usual meaning used in fluid dynamics.

Flow Chart

When the capillary tube based microfluidic model was designed completely in ANSYS Fluent environment for the two pH buffer solutions mixture, number of time steps was selected at first and then iteration limit was given. When the solution got converged for one time step, the solution got updated. After the above process to be converged, the next time step began. In this way, every

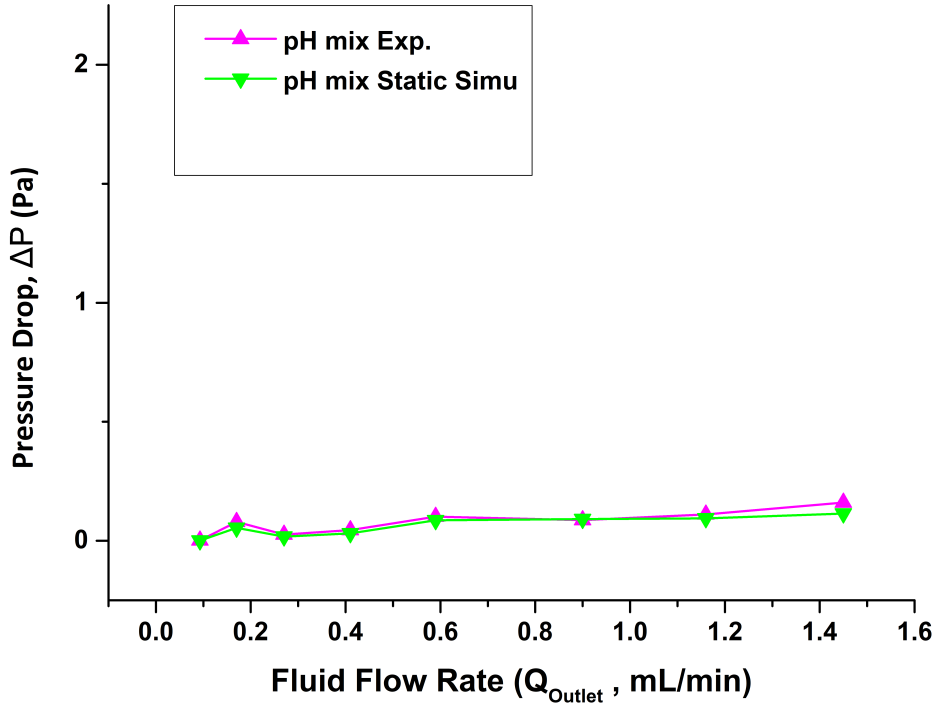


FIGURE 5.2: Validation of numerical model with experimental data for pressure drops at inlets and outlet

time when the consecutive solutions got converged, the next time step began and so on. The flow chart of general procedure of simulation (Fig.5.3) has been stated below:

The important values and conditions used from simulator are described in the following tables (Tables 5.3, 5.4 and 5.5):

Numerical settings

Using powerful commercial computational fluid dynamics (CFD) package of ANSYS Fluent [BGP08; APA19; KCD16b], the numerical simulation was carried out with the 0.001 residual convergence conditions for pressure, density, momentum and 10^{-8} for energy. In general, pressure based solver with absolute velocity for transient time dependent model was used . The fluid was considered to flow in the laminar region. The boundary walls were imposed with no slip

TABLE 5.3: Setup Model and Solver conditions

Solver Type	Pressure Based
Solver velocity formation	Absolute
Time	Transient
2D space	Planar
Models	VOF multiphase model, Energy, Laminar viscous
Materials	Water(liquid) with experimental pH value of substances
Boundary Conditions	Velocity inlet, Pressure outlet, No-slip stationary wall function
Reference Zone	Surface body

TABLE 5.4: Solution conditions

Pressure-velocity Coupling Scheme	Simple Type
Spatial Discretization Gradient	Least squares cell based
Spatial Discretization pressure	PRESTO!
Spatial Discretization momentum	Second order upwind
Spatial Discretization volume fraction	Compressive
Spatial Discretization Energy	Second order upwind
Transient Formulation	First order Implicit
Under-Relaxation factors	Pressure-0.3, Density-1, Body force-1, Momentum-0.7, Vaporization Mass-1, Volume fraction-0.5, Energy-1

TABLE 5.5: Calculation conditions

Initialization type	Hybrid initilization
Time advancement type	Fixed
Time advancement method	User-specified
Number of time steps	20,30,50,100 (as CPU capacity)
Time steps Size(s)	0.001
Max iteration/Time steps	20
Reporting Interval	1
Profile update interval	1

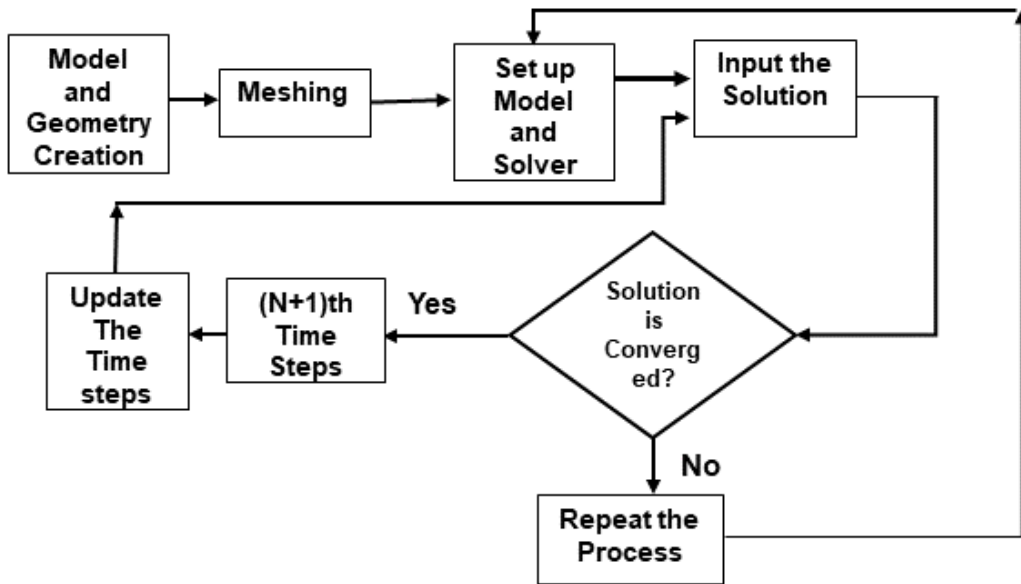


FIGURE 5.3: Flowchart of 2D ANSYS Fluent simulation using fluid dynamics

condition and constant 300 K temperature. The input applied boundary conditions were velocity in inlets for both pH 4 and pH 10 solutions with same given velocity applied at each of two inlets and different densities, viscosities etc. from Table 5.1. The properties of both pH fluids were assigned to a new material section in fluent database. The outlet of mixing pH buffer solution was considered in pressure outlet. Simple scheme for pressure velocity coupling algorithm was used in solution methods. For spatial discretization least square cell-based gradient with PRESTO, pressure and second order upwind momentum for first order implicit were used also in solution methods. The under-relaxation factors in solution controls were taken as a half from default to improved convergence rate. Hybrid initialization was used with 0.001s time steps. Fixed type time advancement with 20 number of time steps for maximum 100 iterations were assigned to calculate. However, the solution was converged within 450 to 800 iterations when the residual reached the limiting point.

TABLE 5.6: Mesh Dependency For Grid-Independent Study Of Validation Using Linear Regression Method

Element Size,mm	Node	Elements	$\Delta P_{mixexp.}(Pa)$ *	$\Delta P_{mixsimu.}(Pa)$
4.5×10^{-2}	12323	12020	0.087	0.01295
5×10^{-2}	10458	10185	0.087	0.086
5.5×10^{-2}	9145	8898	0.087	0.0404
6×10^{-2}	8030	7805	0.087	0.0117
7×10^{-2}	6474	6278	0.087	0.0136
8×10^{-2}	5496	5323	0.087	0.0145

Values of asterik sign (*) indicate the application of the regression method

5.3 Mesh dependency and validation of simulation in CFD environment

5.3.1 Mesh dependency and validation of simulation

The simulation is validated with experimental result of pressure drops in our designed micro fluidic channels of two inlets and one outlet with the deviation range from $\pm 34\%$ to $\pm 4.6\%$. Using $4.5 e^{-5}$, $5 e^{-5}$, $5.5 e^{-5}$, $6 e^{-5}$, $7 e^{-5}$, $8 e^{-5}$ m element sizes with 10 inflation layers in boundary, the model is the mesh properly orthogonal rectangular structure. All the simulation then carried out for $5 e^{-5}$ elements size with 10185 elements as it gave the lowest deviation from the trials. The data estimation using regression method is described in Table 5.2 and Table 5.6. Fig. 5.2 and Fig. 5.4 were drawn graphically for the model validation and mesh dependency [SLL14] respectively.

When two pH buffer fluids via MFC were flushed out through the outlet, outlet itself was opened at the same atmospheric pressure of the outside temperature. With the velocity of two mixed pH fluids via inlets, it was found net mixed product of these fluids through the open space of outlet. Therefore, in reality, final fluidic parameters at the outlet were considered from the mixture of two separate pH fluids and three dimensional diameter based shape of the outlet

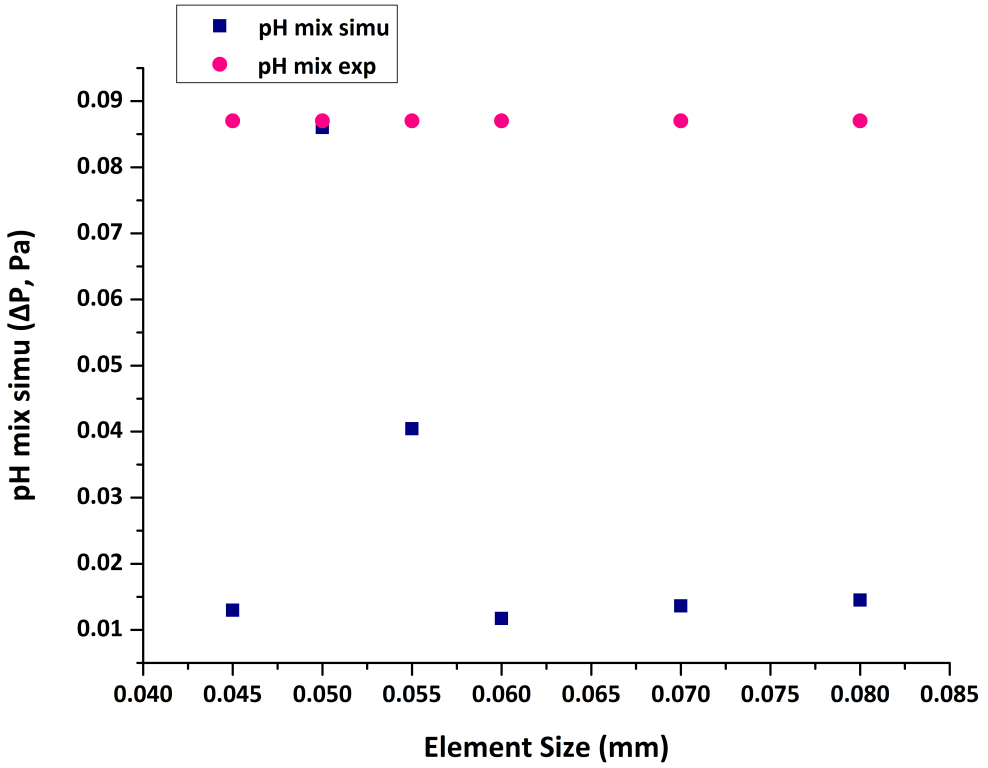


FIGURE 5.4: Mesh dependency for grid-independent study of validation

which was higher than that of each of two inlets. However, in two dimensional simulations, we considered only the fluids flow through the planar surface without taking into consideration the effect of fluids via three dimensional micro flow channels. That is why, the deviations are seemed to be varied from -4.6 % to 34.62 % in the simulation process. The percentage of error of change of pressure drop in between experimental and simulation result is calculated as:

$$(\%)Error = \frac{\Delta P_{outExp.} - \Delta P_{outSimu.}}{\Delta P_{outExp.}} \quad (5.10)$$

On the other hand, for example, from the first measurement of experimental data of Table 4.3, for each of two inlets, total of $(0.1+0.1) = 0.2$ mL/min FFR, we got corresponding net value of 0.17 mL/min FFR at the outlet. This is because of the loss of a significant amount of fluids inside the surface walls of

micro flow channels due to the consideration of a certain measurement time by stopping the flow of fluids. Therefore, to overcome such difficulty in practical case, it was necessary to do linear regression by taking averages of pressure drops at the outlet. Considering the lowest deviation with the experiment, mesh dependency test was applied for the highest 10185 elements carried out by the velocity ranges from 0.26 mm/s to 0.38 mm/s as it gave lowest deviation during the testing process. At these ranges, the deviation from the experimental results showed minimum error to consider for the validation of simulation results.

5.4 Summary

This chapter describes the process of simulation of different viscous pH buffer solutions using CFD based intensive environment to analyze the behavior of hydrodynamic parameters of microfluidic chip from fluid dynamics. Moreover, the simulation was done to compare with the experimental result so that the performance of the microfluidic chip can be evaluated by flowing two pH buffer fluids.

Chapter 6

Digital Filter Design and Testing

6.1 Introduction and Motivation

This chapter introduces with the requirement of doing fast scanning of higher contrast of THz images. Here, for this purpose, it was necessary to use filter in THz imaging process. The reasons of the selection of adaptive digital filter (ADF) [GB15], [Bar+07], [JCM12] over any other filter, are of its computational simplicity, robustness and popular use in biomedical, electrical and communication engineering specially.

6.2 Working Principle of an Adaptive Digital Filter

An ADF adjusts the filter coefficients, followed by the method of an adaptive least mean square (LMS) algorithm. While as a computational device, ADF attempts to model the relationship between two signals in real time in an iterative manner. A sample from a digital input signal $x(n)$ is fed into a device, called an adaptive filter, that computes a corresponding output signal sample $y(n)$ at time n . The output signal is compared to a second signal $d(n)$, called the desired response signal, by subtracting the two samples at time n. This difference

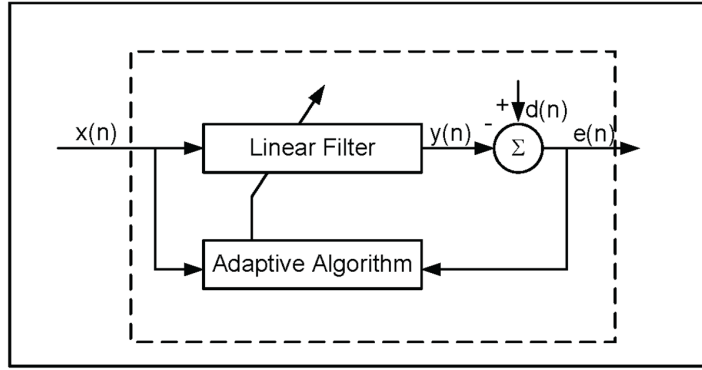


FIGURE 6.1: Functionality of an ADF during the computational operation

signal, given by $e(n) = d(n) - y(n)$ is known as the error signal. The error signal is fed into a procedure which alters or adapts the parameters of the filter from time n to time $(n + 1)$ in a well-defined manner. This proposed LMS algorithm adjusts the coefficients of the linear filter in iterative process to minimize the power of $e(n)$. The LMS does the following arithmetical operations to update the coefficients of an adaptive finite impulse response (FIR) filter [Hay08]:

Step 1:

$$y(n) = \vec{u}^T(n) \cdot \vec{w}_1(n) \quad (6.1)$$

where, $\vec{u}(n)$ is the filter input vector and

$$\vec{u}(n) = x(n)x(n-1)\dots\dots\dots x(n-N+1) \quad (6.2)$$

where, $\vec{w}_1(n)$ is the filter coefficients vector.

Step 2: To calculate the error signal $e(n)$ from the equation;

$$e(n) = d(n) - y(n) \quad (6.3)$$

Step 3: To update the filter coefficients from the equation;

$$\vec{w}_1(n+1) = (1 - \mu)\vec{w}_1(n) + \mu \cdot e(n) \cdot \vec{u}(n) \quad (6.4)$$

where μ denotes the step size (SS) as a gain constant parameter of the ADF. The whole process of adaptation is represented by the oblique arrow that pierces the adaptive filter block in the Fig. 6.1.

6.3 Experimental Set up for ADF's Proper Functioning Check

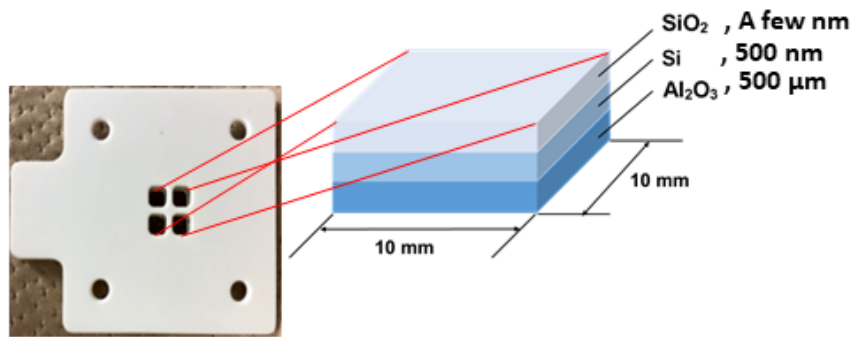


FIGURE 6.2: Sensing plate arrangement for the testing of effectiveness of the ADF

For the integration of the ADF with the TCM system, LMS algorithm using digital signal processing technique has been programmed and implemented in laboratory virtual instrument engineering workbench (LabVIEW®) by analyzing the improvement for capturing higher contrast of THz images. Four wells sensing plate in Fig.6.2 was used to test the proper functioning of the ADF by pouring Milli-Q water solutions onto the sensing plate of each of four wells. The conceptual diagram of such four wells plate with the application of THz electromagnetic wave using the TCM system is shown in Fig.6.3.

The same working principle of section 2.3 and set up of TCM system were used here for this testing except the digital pressure machine, microfluidic chip and samples of chapter 2. From femtosecond laser pulses, two types of laser beams were generated; the pumping and trigger beams. First of all, the alignment of pumping and trigger beams of THz laser was finished for each of the measurement of TCM system. Then, the position of laser was moved by starting the

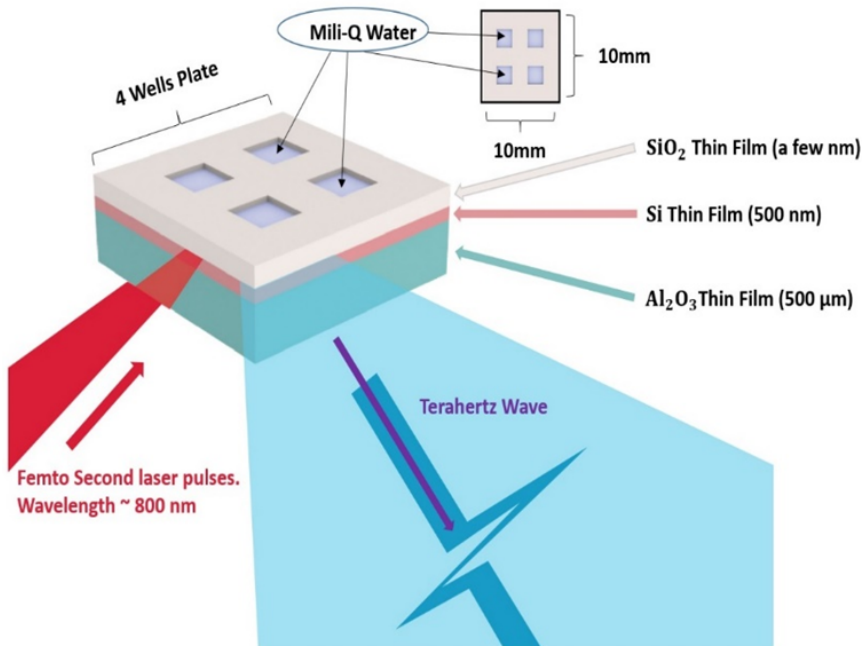


FIGURE 6.3: Conceptual diagram of four wells plate with the application of THz wave

scan of the mili-Q water samples on the sensing plate. The optical signal was detected by the photo conductive antenna, used as a detector. For the identification of the position of peak amplitude of THz data, the delay stage of chopper was used. For choosing the correct sampling frequency, number of samples of signal data to be sampled according to Nyquist sampling theorem, the analog to digital converter (ADC) was programmed in LabVIEW® (section 2.3). Then, using ADF, sampled data were filtered by averaging the raw THz data from the simulation of LabVIEW®. THz imaging data were captured and plotted using personal computer (PC). At the end, the average filtered data were plotted in the form of contour of THz images by measuring points by points of imaging step.

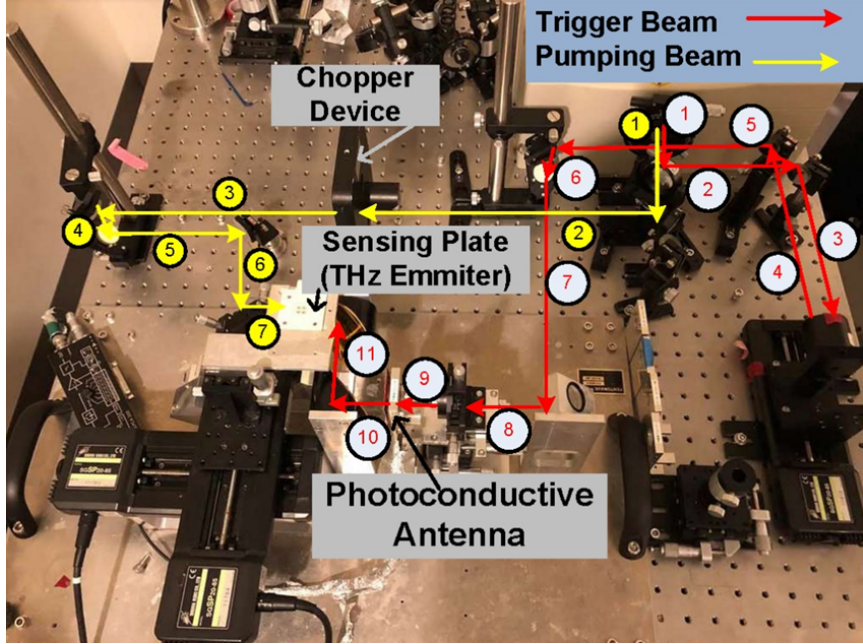


FIGURE 6.4: Optical set up of TCM system to start measurement for this project

6.4 Statistical Analysis of Characteristic Curve of ADF

The quantitative analysis of the characteristic curve of ADF was plotted from the variation of standard deviation (SD) with respect to step size (SS) with the optimization of step size as a gain constant-one of vital parameters of the filter [Ahm+19]. From the algorithm of ADF, it can be said that convergence speed is used for adjusting the minimum error with the main input signal. The aim of this project is to fix the optimum condition level of convergence speed of LMS algorithm with respect to step size from which the total measurement time of the THz imaging was reduced without loosing the original scanning speed of TCM by internally applied ADF. Fig.6.5 shows standard deviation versus step size curve where the time constants (TC) of lock-in-amplifier were set as 30 ms and 100 ms.

From the computational analysis of LMS algorithm, 0.001, 0.01, 0.05, 0.5, 1,1.5,

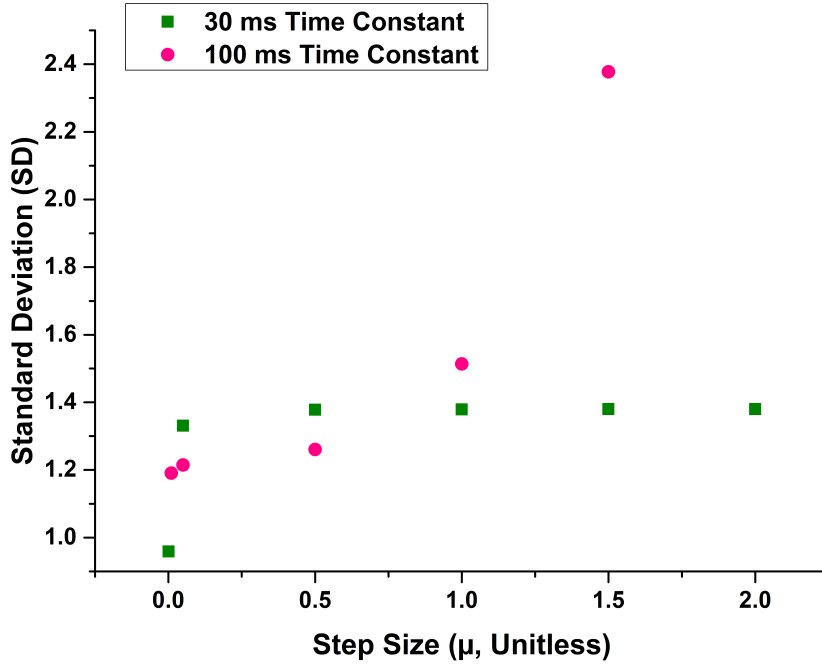


FIGURE 6.5: Standard deviation versus step size curve for evaluating the characteristics of 100 ms and 30 ms TC of lock-in amplifier with the application of ADF

and 2 step size values were given as input data to calculate corresponding standard deviation values so that optimum value of standard deviation would be fixed for the high precision based performance of the ADF with the higher quality of contrast of THz images along with the unchanged original scanning speed of the TCM system.

From the quantitative analysis, step size's value of 0.001 was chosen as an optimum value for getting higher contrast of THz images by analyzing parameters' variation of the filter. Therefore, the performance of the ADF was evaluated in terms of the standard deviations of images as a function of step sizes of the filter and plotted in Fig.6.5.

In Fig.6.5, for two different family of curves, the standard deviations of data of the signal were not saturated for 100 ms rather than increased monotonically with larger values of step sizes. On the contrary, the curve for 30 ms exhibited

with the criteria of early saturation even at standard deviation value of 0.01. Therefore, during the analysis of two qualitative results, for the step size of 0.001 of ADF, higher contrast was achieved with the reduction of total measurement time of TCM by taking into the consideration of the optimum level issue of standard deviation. By considering this fact, the data captured with ADF were (a) contrast of 0.74 for 30ms time constant of lock-in-amplifier corresponding to the standard deviation value of 0.96 and, (b) contrast of 0.73 for 100ms time constant of lock-in-amplifier corresponding to the standard deviation value of 1.19. From the basic principle of lock-in-amplifier, time constant is inversely proportional to the bandwidth of low pass filter (LPF) integrated with the lock-in-amplifier. Therefore, with the lower value of the time constant, the bandwidth of LPF became wider with lower signal-to-noise-ratio (SNR) and faster measurement. Higher value of time constant subjects to narrower bandwidth of low pass filter with higher signal-to-noise ratio and slower measurement fact. The designed adaptive digital filter worked on 30 ms time constant brought early saturation, compared with 100 ms time constant. Because in the case of 30 ms, ADF got much wider bandwidth to collect more signal information by adapting with the input THz signal to reduce the degree of standard deviation and minimize error according to its working principle followed by LMS algorithm [Ahm+19].

6.5 Determination of Contrast of THz Images

For the performance evaluation in terms of the quality of images using ADF, The following process was used to estimate the standard deviation and contrast of the THz images:

Firstly, the values of pixels inside and outside of the well were taken, that was marked by the red-yellow dashed squares region in the graphic of Fig.6.6.

Secondly, calculation for the determination of standard deviations of the pixels were performed in the both inside and outside of wells

Thirdly, to evaluate the contrast of the images, the values of pixels inside and outside of the wells I_{max} and I_{min} were taken respectively and estimated by:

$$\text{contrast} = \frac{I_{\text{max.}} - I_{\text{min.}}}{I_{\text{max.}} + I_{\text{min.}}} \quad (6.5)$$

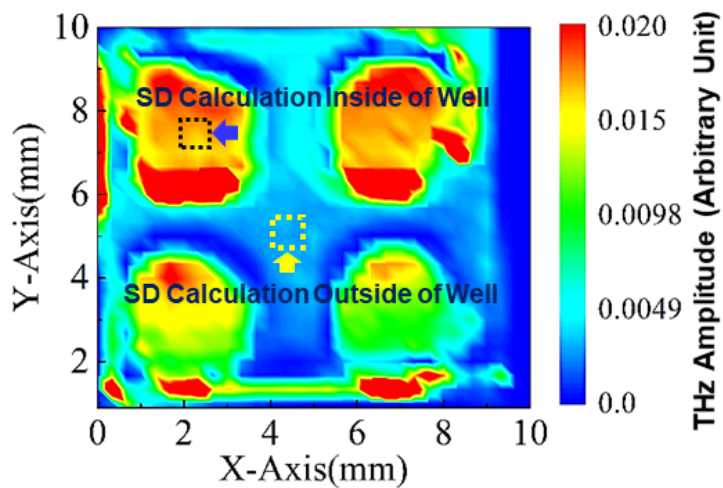


FIGURE 6.6: Calculation and estimation of standard deviation for several pixels of data of THz images inside the upper of the well and outside region of the Well onto sensing plate

6.6 Qualitative Analysis of Contrast with and without Filter

The quality of contrast without and with filter are estimated in this section. In Table I, the values of contrast with filter are more than double than that of without filter. Therefore, to capture higher contrast of THz images with higher scanning speed, the primarily chosen contrast values are 0.74 and 0.73 for 30 ms and 100 ms time constant respectively. However, the aim was to keep standard deviation values as lower as possible with respect to the step sizes of the ADF in parallel with the target of higher quality of contrast of THz images. Therefore,

TABLE 6.1: Estimation of Standard Deviation and Contrast of THz Images

With or Without Filter	100ms Time Constant			30ms Time Constant		
	SS	SD	Contrast	SS	SD	Contrast
Without Filter	N/A	0.01	0.32	N/A	0.07	0.34
With Filter	0.001	1.19	0.73	0.001	0.96	0.74

the recommendation here is the lowest value of standard deviation of 0.96 with respect to step size of 0.001 of the filter whose contrast is of 0.74 for 30ms time constant of the lock-in-amplifier. As a result, contrast of THz images was improved notably. Moreover, from the view of the time constant, the contrast did not compromise by decreasing the time constant from 100 ms to 30 ms that suggested the reduction of the total measurement time of THz data.

The statistical analysis and calculation without and with filter for the standard deviations and the contrast of images are shown in the Table 6.1.

6.7 Contour of THz Images with and without Filter

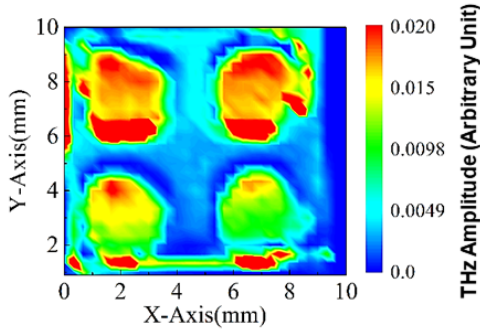


FIGURE 6.7: Contour of THz Image with filter for the contrast of 0.73, TC 100 ms

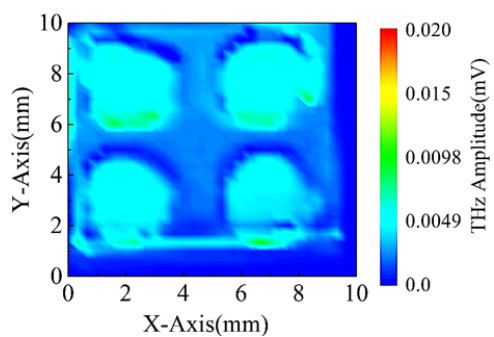


FIGURE 6.8: Contour of THz Image without filter for the contrast of 0.32, TC 100 ms

The outcome of THz images with and without filter for 30 ms time constant of lock-in-amplifier are plotted in Fig.6.7 and Fig.6.8 respectively. Moreover, the contour of THz images for 100 ms time constant of lock-in-amplifier are

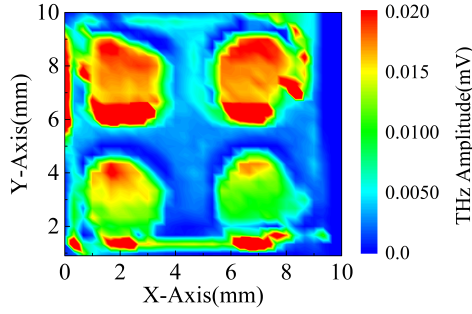


FIGURE 6.9: Contour of THz Image with filter for the contrast of 0.74, TC 30 ms

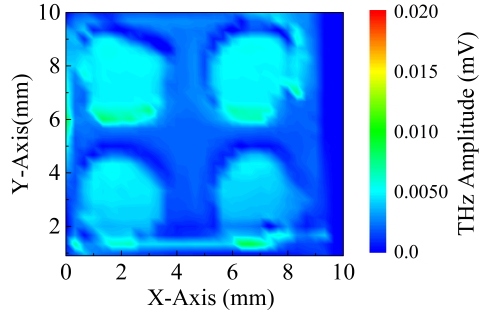


FIGURE 6.10: Contour of THz Image without filter for the contrast of 0.34, TC 30 ms

plotted in Fig.6.9 and Fig.6.10 respectively. During the experiment, two upper wells of the sensing plate of above mentioned all figures, were poured with 5 μL mili-Q water solutions, while lower two wells were poured with 1 μL mili-Q water solutions.

6.7.1 Data Acquisition of THz Images

THz data obtained from the experiment, were averaged without and with filter using LabVIEW® simulation. By setting lock-in-amplifier time constants of 30 ms and 100 ms, with and without filter, two-stage controlling LabVIEW® simulation was used to adjust ADC's number of samples data = 100, sampling frequency, $\text{fs} = 1\text{kHz}$, followed by the Nyquist sampling theorem for the time interval of 1 ms in case of each measurement. The total acquisition time for measurement in both cases = (time constant of Lock-in-amplifier + No. of samples \times time interval of ADC).

In case of (10 mm x 10 mm) dimensions of sensing plate, 6300 points = 1 mm was programmed using LabVIEW® with the resolution of $333\mu\text{m}$ for each of pixel data in order to scan total images by THz laser. Thus, during the experiment with (10 mm x 10 mm) dimensional sensing plate, THz laser scanned 63000 by 63000 points for each of measurement steps to capture each of THz images

of Fig.6.7 and Fig.6.8. Therefore, ADF was successfully tested the sample of Mili-Q water inside the four wells by recording higher contrast of THz images.

6.8 Advantages of an Adaptive Digital Filter

Using least mean square (LMS) algorithm, an ADF was designed and simulated by LabVIEW®. The causes of choosing ADF over any other filter, are for the reasons below: (i) One of ADF's parameters, convergence speed (CS) manages optimal solution with iteration method (ii) To possess miss-adjustment ability for measuring the amount by which the final value of Mean Square Error (MSE), averaged over a gross calculation of filtering, deviated from the mean square error (iii) To have tracking capability by following statistical variations in the environment of a random, non-stationary, time varying signalm, (iv) ADF can be able to adjust even small estimation errors from the small disturbances of any source that imply its robustness (v) Compared with other methods of signal processing filters, it has computational simplicity.

6.9 Summary

This chapter experimentally observed that the filter would improve the contrast double without compromising existing scanning speed of the TCM system. In addition, total measurement time was reduced from the optimum value of standard deviation corresponds to the step size of ADF.

Chapter 7

Results and Discussions

7.1 Introduction

Transport of fluids [HSR13] phenomena on the micro scale level have achieved particular importance owing to the progressive demand for more efficient and sustainable processes. Especially, to co-relate the nano- and micro technologies that require a clear understanding of multi-scale coherence. The recent advancement in micro-fluidic and nano-fluidic technologies have been moving forward in parallel ways by the advancement in methods for the direct optical measurement of transport of fluids phenomena on these scales. A lot of methods for micro-scale flow visualization have been employed and examined since the late 1990s for fulfilling the better spatial resolution criteria. However, the sharp spatial resolution criteria is still a hot cake to capture the best images of the internal fluidic reactions of chemical and biological solutions.

Even if the flow conditions of chemical and biological solutions on the microscale level are almost laminar owing to the smaller dimensions and therefore, high accuracy are applicable for the numerical simulations, there are some remarkable causes for the basic necessity of the visualization [HSR13] of the experimental flow of the fluids. In most of the cases, for example, data on chemical media such as diffusion coefficients, reaction rates and the accurate data of geometries

and wall conditions of micro flow channels are not be able to find out. Furthermore, through the micro flow channels, chemical reactions are not calculable to date for the interaction between mass transport and conversion, especially in case of catalytic processes have taken place simultaneously. As a result, the visualization of micro-scale flow is an effective method and tool to understand and optimize the micro flow channels in micro scales. For the visualization of internal microfluidic reactions in micro-scale level convincingly, most measurement techniques make use of a microscope [HSR13] to get suitable spatial resolution. Therefore, optical access is necessary in order to allow a view into the internal micro flow channels without interrupting the conditions of the flow of fluids. Here, THz image sensing technology using THz chemical microscope with $0.8\mu m$ wavelength meets up the demand of sharp spatial resolution criteria.

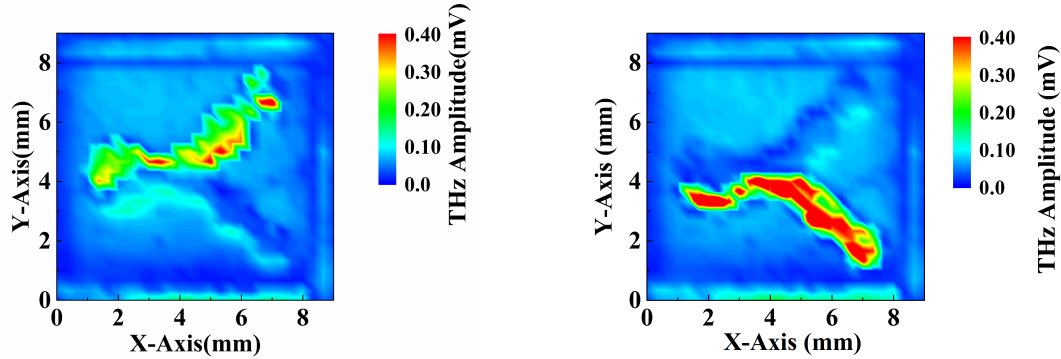


FIGURE 7.1: THz captured data for the interaction of pH 4 and 10 buffer solutions at 0.07 mL/min fluid flow rate

FIGURE 7.2: THz captured data for the interaction of pH 4 and 10 buffer solutions at 0.15 mL/min fluid flow rate

Moreover, in this dissertation, ANSYS Fluent software for computational fluid dynamics (CFD) simulation was used to explain not only the experimental flow phenomena but also predict new flow phenomena, providing a better realization of the chemical and biological micro-environment and fundamentals of microfluidic flows in case of manipulation and analysis. The objective of this ANSYS based CFD simulation is to simulate small-scale fluid flow with the visualization of the interaction of different fluids inside the internal micro-environment

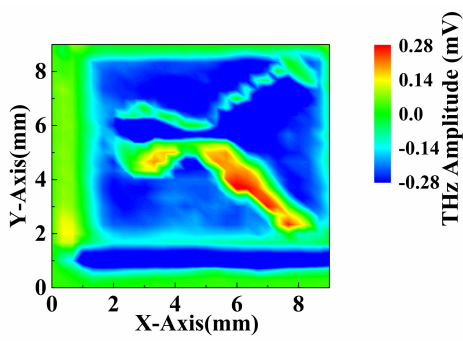


FIGURE 7.3: THz captured data for the interaction of pH 4 and 10 buffer solutions at 0.25 mL/min fluid flow rate

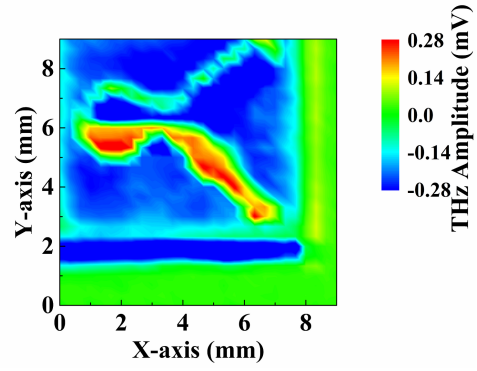


FIGURE 7.4: THz captured data for the interaction of pH 4 and 10 buffer solutions at 0.4 mL/min fluid flow rate

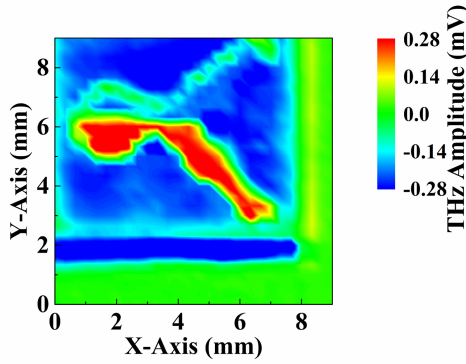


FIGURE 7.5: THz captured data for the interaction of pH 4 and 10 buffer solutions at 0.7 mL/min fluid flow rate

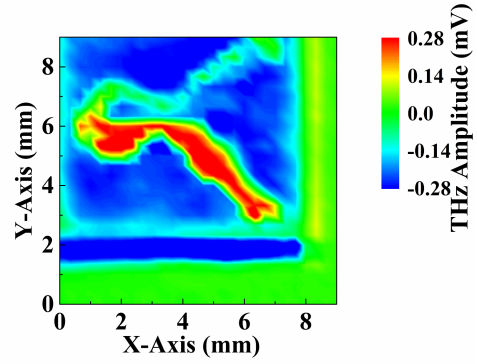


FIGURE 7.6: THz captured data for the interaction of pH 4 and 10 buffer solutions at 0.8 mL/min fluid flow rate

using volume of fluid (VOF) [Eri05a] method, followed by the THz laser scanned visualization method. In addition, from experimental measurement data of different microfluidic parameters, the experimental results were validated with the simulation generated data to investigate optimal chip design, flow fundamentals and possible applications of microfluidic lab-on-a-chip systems.

7.1.1 THz Imaging results

During the experiment, THz data were recorded to capture the interaction of two different viscous pH=4 and 10 buffer solutions through the micro flow channels of the designed microfluidic chip. The contour of THz Images driven by the THz laser scanned TCM system were plotted for different fluid flow rates

(viz. 0.1, 0.15, 0.25, 0.4, 0.6 mL/min etc.) that were applied to each of two inlet wells of micro flow channels as input data. For each experimental reading, using syringe-connected two tubes, same two set values of fluid flow rate from digital pressure machine were applied at each of two inlet wells of the microfluidic chip. The captured image maps of internal microfluidic reactions of two above mentioned pH solutions through the fabricated micro flow channels were shown in Fig. 7.1, Fig. 7.2, Fig. 7.3, Fig. 7.4, Fig. 7.5 and Fig. 7.6 in the form of THz images.

7.1.2 2D ANSYS Fluent simulation results

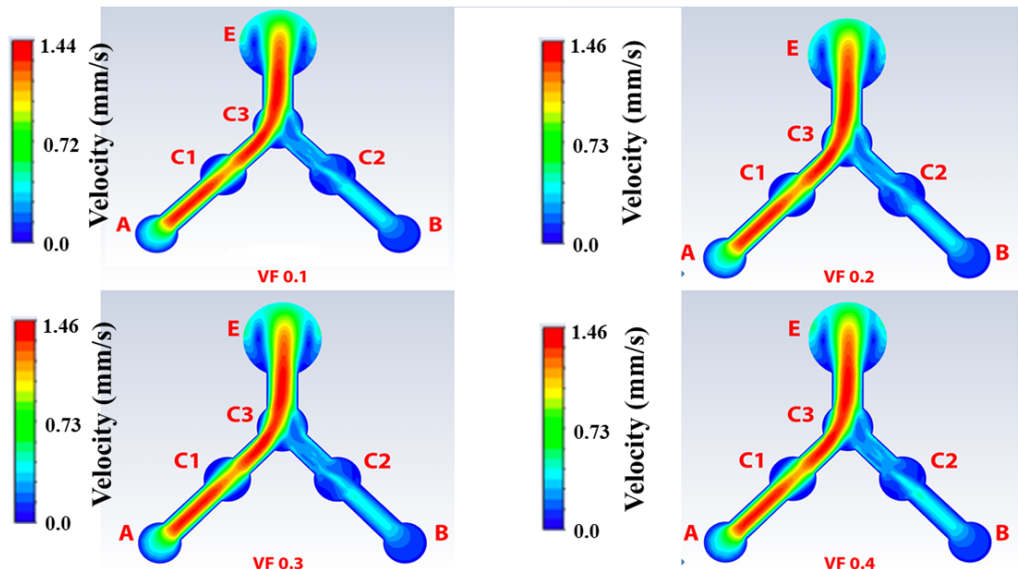


FIGURE 7.7: Same set of input velocity applied to each of two inlet wells with respect to different increased volume of fraction; same input velocity, 0.064 m/s applied at A and B points for two pH solutions.

Here, the change of volume of fractions (VF) using VOF [Eri05a] method is utilized to predict the nature of two immiscible phases of fluids flow by evaluating the influence of such multi-phase modeling approach on the flow of pH 4 and 10 viscous acidic and base fluids.

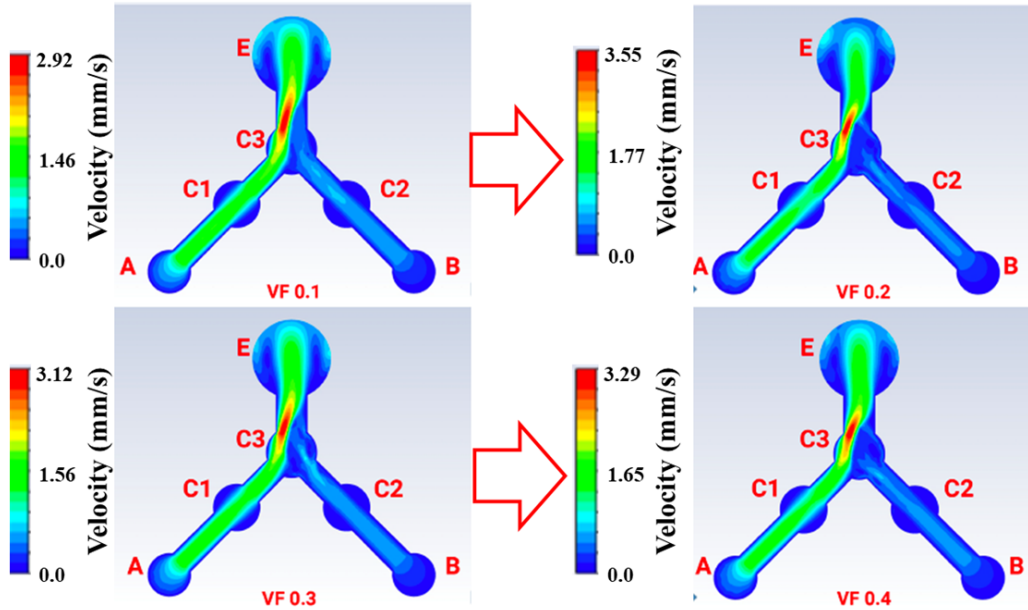


FIGURE 7.8: Same set of input velocity applied to each of two inlet wells with respect to different increased volume of fraction; same input velocity, 0.096 m/s applied at A and B points for two pH solutions.

Using ANSYS Fluent for CFD simulation, with the increased values of VF, different velocity profiles-based flow of solutions were simulated in Fig. 7.7 and Fig. 7.8 from inlet points via intermediate points C_1 and C_2 and common junction well point, C_3 to exit point E . In Fig. 7.7 and Fig. 7.8 , based on the concept of fluid dynamics, two fluid flow solutions didn't mix with each other by flowing through each of two layers separately. Therefore, $pH=4$ and $pH=10$, two different viscous buffer solutions exhibited the laminar nature of fluid flow. Two different viscous solutions travelling through the micro flow channels, created friction at the boundaries of micro flow channels that in turn created a bit speed tendency to deflect slightly from the spontaneous flow of fluid flow solutions. The higher the viscosity of a fluid, the higher the tendency of the deflection of the speed of fluid flow was observed, with the increased fluid flow rates as well. Therefore, $pH=10$ solution denotes the yellowish and red mixed color marked velocity profiles in Fig. 7.7 and Fig. 7.8 and its viscosity $0.58 \text{ mPa}\cdot\text{s}$ is higher than that of $pH=4$ solution. $pH=4$ solution mapped with the surface of its flow

path which is shown in the simulated velocity profiles. Moreover, the pH=10 velocity profiles possess higher dragging effect owing to the frictional force experienced inside the internal layers of micro flow channels than that of pH 4 solution.

In Fig. 7.8, with the increased values of VF, the velocity profile path showed so slight change for the same applied velocity (0.096 m/s corresponding to 0.15 mL/min) at each of A and B points. Similarly, in Fig. 7.7, same input velocity of 0.064 m/s corresponding to 0.1 mL/min fluid flow rate for two different viscous pH solutions was applied at each of “A” and “B” points, with the increased values of VF. However, in Fig. 7.7, the simulated data do not show any appreciable change inside the paths of velocity profiles even though the change of VF values controlled data. It signifies that velocities profiles are nearly same with the increased values of VF. As a result, the simulated data with optimum velocity 0.064 m/s corresponding to 0.1 mL/min of Fig. 7.7 would be countable for the almost ideal fluid flow patterns through the micro flow channels of the simulated microfluidic chip. The reason is that they show consistent behavior of fluids flow with the outcome of almost same velocity profiles of laminar nature in spite of the increased values of VF.

7.2 Analysis of Velocity Profiles obtained from ANSYS Fluent

According to the previous section’s assigned notation of Fig. 7.7 and Fig. 7.8, pH=4 and 10 viscous acidic and base solutions were inserted into A and B points respectively in order to compare the velocity-based flow patterns inside the microfluidic structure from simulation and experimental measured velocity profiles. The objective of this discussion is to satisfy the simulation results based on continuity equation of fluid dynamics.

Fig. 7.7 and Fig. 7.8 indicate different profiles of velocities inside the micro flow channels at the starting same input velocity of 0.064 m/s and 0.096 m/s respectively. In the design of the microfluidic chip, the dimensions that were used, same all dimensions were used during the simulation process. In Fig. 7.7 and Fig. 7.8, the diameters of different points were $A_{dia.} = B_{dia.} = 1.1$ mm, $C_{1dia.} = C_{2dia.} = 1.2$ mm and $E_{dia.} = 2$ mm. In Fig. 7.7, through A and B inlet points,in each case, initial velocity showed high value and through C_1 and C_2 points, velocity showed low profiles. The reason is that the diameter of each of C_1 and C_2 of that parts of the chip was larger than that of each of A and B. When fluid travelled through the C_1 and C_2 points, velocity of fluid increased again because of the smaller diameter of rectangular path provided channel. At $C_{3dia.} = 1.2$ mm point, here the larger diameter was designed. Therefore, at this common junction point C_3 , the velocity of pH=4 fluid's flow was dropped. Moreover,the other pH=10 fluid also travelled this common junction point that surely affected the velocity of pH=4 fluid due to the heat transfer, pressure etc. phenomena. After leaving from C_3 point, it was designed here a rectangular path of 0.8 mm diameter that boosted to increase the velocity of mixed two pH fluids again. At the outlet point E, velocity again dropped due to the larger diameter of 2mm than any other dimensional path of full fluid flow channels.

7.3 Summary

In this chapter, THz generated laser scanned the internal microfluidic reactions to visualize the chemical reactions with sharp spatial resolution to get the best outcome of the this project. Then, ANSYS Fluent with CFD simulation was executed to analyze the flow patterns of fluid flow solutions on the basis of fluid dynamics.

Chapter 8

Conclusion and Future Works

This dissertation proposed a THz imaging technique to characterize and observe the flow of different pH buffer solutions through the designed microfluidic chip where the testing of pH level maintained liquid foods, blood samples analysis to observe any pH variation can be possible in our daily life. From technical point of view, the performance of the designed microfluidic chip was evaluated in terms of the analysis of hydrodynamic parameters of fluid dynamics that actually controls the performance of the microfluidic chip. Moreover, an universal digital filter is proposed in this dissertation to test its effectiveness to capture the imaging maps of biological and chemical solutions shapely. From this dissertation, it was improved the contrast of the THz images using such filter.

Chapter 1 introduces the recent advancement of this project work, motivation, background, and contributions of the study. **Chapter 2** describes and defines the mechanism of THz generation and detection principles. **Chapter 3** introduces the fabrication, manufacturing process of PDMS designed microfluidic chip. In **Chapter 4**, the hydrodynamic parameters were calculated from fluid dynamics, experimented using the designed microfluidic chip to find out the characteristics of different internal microfluidic parameters. **Chapter 5** contains the ANSYS Fluent software based CFD simulation to evaluate the

experimental result with the simulation result so that the performance of the designed microfluidic chip can be improved in a appreciable manner. **Chapter 6** explains the proposed adaptive digital filter design for the improvement of the contrast of the THz images so that the TCM system can allow faster measurement of chemical and biological samples. **Chapter 7** is very much crucial to find the outcome of this dissertation so that one can realize the achievement of this dissertation fully. Here, the THz imaging maps of interaction of pH buffer solutions were captured and discussed from the technical view of fluid dynamics. Moreover, CFD based simulation results show the visualization of the two pH buffer solutions through the internal micro flow channels of the designed microfluidic chip.

As future works, more complex structure of the microfluidic chip will be designed to test more than two chemical solutions at a time through more than two internal micro flow channels of the designed microfluidic chip. Thus, from the interaction of more than two chemical and biological solutions, it can be possible to visualize the interaction of more than two solutions in the form of THz images. Apart from this, the designed adaptive filter's version will be improved by following different methodologies of digital signal processing techniques so that the faster scanning of biological and chemical solutions using THz laser can be possible. The ultimate target is to use such microfluidic structures for showing the contribution in real life applications of biomedical engineering. Moreover, fluid mechanics design engineers have been searching for higher spatial resolution criteria using so many optical arrangements to capture sharp microfluidic reactions based images. However, still they have achieved maximum of $6.47 \mu\text{m}$ spatial resolution [Tor+20] by applying optical method for the measurement of heat and flow of fluid solutions. The THz technology used here already achieved $333 \mu\text{m}$ spatial resolution criteria for each of pixel of THz image to capture the internal microfluidic reactions that is more than 50 times

higher than that of optical measurement by the fluid mechanics engineers. In future, we can achieve more sharp spatial resolution by modifying the optical set up of the TCM system for the faster scanning and movement of THz laser. Moreover, the filter's moderate version will be used for capturing the faster scanning of movie clips, faster chemical reactions made solutions in future.

Bibliography

- [Ahm+19] Feroz Ahmed, Tatsuki Kamiya, Yuki Maeno, Toshihiko Kiwa, Kenji Sakai, and Keiji Tsukada. “Improvement of contrast of Terahertz Images of a Terahertz Chemical Microscopy using Adaptive Digital Filter”. In: *2019 International Conference on Computer, Communication, Chemical, Materials and Electronic Engineering (IC4ME2)*. IEEE. 2019, pp. 1–4.
- [Ahm+21] Feroz Ahmed, Atsuya Mahana, Katsuya Taniizumi, Jin Wang, and Kenji Sakai. “Terahertz imaging technique for monitoring the flow of buffer solutions at different pH values through a microfluidic chip”. In: *Japanese Journal of Applied Physics* (2021).
- [APA19] Masoud Arabghahestani, Sadegh Poozesh, and Nelson K. Akafuah. “Advances in Computational Fluid Mechanics in Cellular Flow Manipulation: A Review”. In: *Applied Sciences* 9.19 (2019). ISSN: 2076-3417. URL: <https://www.mdpi.com/2076-3417/9/19/4041>.
- [B81] “Simulation tools for lab on a chip research: advantages, challenges, and thoughts for the future”. In: *Lab Chip* 8 (9 2008), pp. 1424–1431. DOI: 10.1039/B812596C. URL: <http://dx.doi.org/10.1039/B812596C>.

- [Bar+07] Jennifer Baraniak, Johann Hauer, Norbert Schuhmann, and Günter Leugering. “Implementation of adaptive filters for biomedical applications”. In: *Russian-Bavarian Conference on Bio-Medical Engineering*. Citeseer. 2007, p. 169.
- [BGP08] David A Boy, Frederic Gibou, and Sumita Pennathur. “Simulation tools for lab on a chip research: advantages, challenges, and thoughts for the future.” In: *Lab on a Chip* 8.9 (2008), pp. 1424–1431.
- [BL17] Nathalie Brandenberg and Matthias P. Lutolf. In: *Biology and Engineering of Stem Cell Niches*. Boston: Academic Press, 2017, pp. 429 –442. ISBN: 978-0-12-802734-9. DOI: <https://doi.org/10.1016/B978-0-12-802734-9.00027-5>.
- [BLL06] David N Breslauer, Philip J Lee, and Luke P Lee. “Microfluidics-based systems biology”. In: *Molecular Biosystems* 2.2 (2006), pp. 97–112.
- [BMW02] David J. Beebe, Glennys A. Mensing, and Glenn M. Walker. “Physics and Applications of Microfluidics in Biology”. In: *Annual Review of Biomedical Engineering* 4.1 (2002), pp. 261–286.
- [Bor+18] Jeffrey T Borenstein, Vishal Tandon, Sarah L Tao, and Joseph L Charest. *Microfluidic cell culture systems, ch.1, 2nd ed., p. 3*. Elsevier, 2018.
- [Bur02] Mark A Burns. “Everyone’s a (future) chemist”. In: *Science* 296.5574 (2002), pp. 1818–1819.

- [Che+08] Pu Chen, Xiaojun Feng, Wei Du, and Bi-Feng Liu. “Microfluidic chips for cell sorting”. In: *Front Biosci* 13 (2008), pp. 2464–2483.
- [CK07] Taek Dong Chung and Hee Chan Kim. “Recent advances in miniaturized microfluidic flow cytometry for clinical use”. In: *Electrophoresis* 28.24 (2007), pp. 4511–4520.
- [Cul+14] Christopher T Culbertson, Tom G Mickleburgh, Samantha A Stewart-James, Kathleen A Sellens, and Melissa Pressnall. “Micro total analysis systems: fundamental advances and biological applications”. In: *Analytical chemistry* 86.1 (2014), pp. 95–118.
- [CWL06] Dino Di Carlo, Liz Y. Wu, and Luke P. Lee. “Dynamic single cell culture array”. In: *Lab Chip* 6 (11 2006), pp. 1445–1449. DOI: 10.1039/B605937F. URL: <http://dx.doi.org/10.1039/B605937F>.
- [Dan+19] Mihai Danciu, Teodora Alexa-Stratulat, Cipriana Stefanescu, Gianna Dodi, Bogdan Ionel Tamba, Cosmin Teodor Mihai, Gabriela Dumitrita Stanciu, Andrei Luca, Irene Alexandra Spiridon, Loredana Beatrice Ungureanu, Victor Ianole, Irina Ciortescu, Catalina Mihai, Gabriela Stefanescu, Ioan Chirilă, Romeo Ciobanu, and Vasile Liviu Drug. “Terahertz Spectroscopy and Imaging: A Cutting-Edge Method for Diagnosing Digestive Cancers”. In: *Materials* 12.9 (2019). ISSN: 1996-1944. DOI: 10.3390/ma12091519. URL: <https://www.mdpi.com/1996-1944/12/9/1519>.
- [DKC15] Guangtao Duan, Seiichi Koshizuka, and Bin Chen. “A contoured continuum surface force model for particle methods”. In: *Journal of Computational Physics* 298 (2015), pp. 280 –304. ISSN: 0021-9991. DOI: <https://doi.org/10.1016/j.jcp.2015.06.004>.

URL: <http://www.sciencedirect.com/science/article/pii/S0021999115003836>.

- [Dor+05] Kevin D Dorfman, Max Chabert, Jean-Hugues Codarbox, Gilles Rousseau, Patricia De Cremoux, and Jean-Louis Viovy. “Contamination-free continuous flow microfluidic polymerase chain reaction for quantitative and clinical applications”. In: *Analytical chemistry* 77.11 (2005), pp. 3700–3704.
- [Eas+06] Christopher J Easley, James M Karlinsey, Joan M Bienvenue, Lindsay A Legendre, Michael G Roper, Sanford H Feldman, Molly A Hughes, Erik L Hewlett, Tod J Merkel, Jerome P Ferrance, et al. “A fully integrated microfluidic genetic analysis system with sample-in-answer-out capability”. In: *Proceedings of the National Academy of Sciences* 103.51 (2006), pp. 19272–19277.
- [Eri05a] D. Erickson. “Towards numerical prototyping of labs-on-chip: modeling for integrated microfluidic devices”. In: *Microfluidics and Nanofluidics* 1 (2005), pp. 301–318.
- [Eri05b] David Erickson. “Towards numerical prototyping of labs-on-chip: modeling for integrated microfluidic devices”. In: *Microfluidics and Nanofluidics* 1.4 (2005), pp. 301–318.
- [Flu+11] ANSYS Fluent et al. “Anssys fluent theory guide”. In: *ANSYS Inc., USA* 15317 (2011), pp. 724–746.
- [GB15] Pankaj Gupta and Poonam Beniwal. “Adaptive filters algorithms: a performance comparison”. In: *Int. J. Eng. Res. Gen. Sci* 3.4 (2015), pp. 2091–2730.

- [GGBY16] Navid Ghorashian, Sertan Katal Gökçe, and Adela Ben-Yakar. “Microfluidic Systems for Whole-Animal Screening with *C. elegans*”. In: *Micro- and Nanosystems for Biotechnology*. John Wiley Sons, Ltd, 2016. Chap. 10, pp. 245–272. ISBN: 9783527801312. DOI: <https://doi.org/10.1002/9783527801312.ch10>.
- [Gre+09] James V. Green, Tatiana Kniazeva, Mehdi Abedi, Darshan S. Sokhey, Mohammad E. Taslim, and Shashi K. Murthy. “Effect of channel geometry on cell adhesion in microfluidic devices”. In: *Lab Chip* 9 (5 2009), pp. 677–685. DOI: 10.1039/B813516A. URL: <http://dx.doi.org/10.1039/B813516A>.
- [GYF04] Jian Gao, Xue-Feng Yin, and Zhao-Lun Fang. “Integration of single cell injection, cell lysis, separation and detection of intracellular constituents on a microfluidic chip”. In: *Lab on a Chip* 4.1 (2004), pp. 47–52.
- [Han+06] JW Handley, Netta Cohen, RD Boyle, and Elizabeth Berry. “An empirical analysis of noise in pulsed terahertz systems”. In: *Fluctuation and Noise Letters* 6.01 (2006), pp. L65–L76.
- [Hay08] Simon S Haykin. *Adaptive filter theory*. Pearson Education India, 2008.
- [He2] “Far-infrared signature of animal tissues characterized by terahertz time-domain spectroscopy”. In: *Optics Communications* 259.1 (2006), pp. 389 –392. ISSN: 0030-4018. DOI: <https://doi.org/10.1016/j.optcom.2005.08.029>. URL: <http://www.sciencedirect.com/science/article/pii/S0030401805008618>.

- [HES13] Hanaa M. Hegab, Ahmed ElMekawy, and Tim Stakenborg. “Review of microfluidic microbioreactor technology for high-throughput submerged microbiological cultivation”. In: *Biomicrofluidics* 7.2 (2013), p. 021502. DOI: 10.1063/1.4799966. eprint: <https://doi.org/10.1063/1.4799966>. URL: <https://doi.org/10.1063/1.4799966>.
- [HN81] Cyril W Hirt and Billy D Nichols. “Volume of fluid (VOF) method for the dynamics of free boundaries”. In: *Journal of computational physics* 39.1 (1981), pp. 201–225.
- [HSR13] Marko Hoffmann, Michael Schlüter, and Norbert Räßiger. “Microscale Flow Visualization”. In: *Micro Process Engineering*. John Wiley Sons, Ltd, 2013. Chap. 4, pp. 93–115. ISBN: 9783527631445. DOI: <https://doi.org/10.1002/9783527631445.ch4>.
- [JCM12] Yuzhong Jiao, Rex YP Cheung, and Mark PC Mok. “Modified log-lms adaptive filter with low signal distortion for biomedical applications”. In: *2012 Annual International Conference of the IEEE Engineering in Medicine and Biology Society*. IEEE. 2012, pp. 5210–5213.
- [Jeo+13] Kiyoung Jeong, Yong-Min Huh, Sang-Hoon Kim, Yeonji Park, Joo-Hiuk Son, Seung Jae Oh, and Jin-Suck Suh. “Characterization of blood using terahertz waves”. In: *Journal of Biomedical Optics* 18.10 (2013), pp. 1 –6. DOI: 10.1117/1.JBO.18.10.107008. URL: <https://doi.org/10.1117/1.JBO.18.10.107008>.

- [Kat19] Nikolaos D. Katopodes. “Chapter 12 - Volume of Fluid Method”. In: *Free-Surface Flow*. Ed. by Nikolaos D. Katopodes. Butterworth-Heinemann, 2019, pp. 766 –802. ISBN: 978-0-12-815485-4.
- [KCD16a] “Chapter 4 - Conservation Laws”. In: *Fluid Mechanics (Sixth Edition)*. Ed. by Pijush K. Kundu, Ira M. Cohen, and David R. Dowling. Sixth Edition. Boston: Academic Press, 2016, pp. 109 –193. ISBN: 978-0-12-405935-1.
- [KCD16b] “Chapter 6 - Computational Fluid Dynamics”. In: *Fluid Mechanics (Sixth Edition)*. Ed. by Pijush K. Kundu, Ira M. Cohen, and David R. Dowling. Sixth Edition. Boston: Academic Press, 2016, pp. 227 –291.
- [KCD16c] “Chapter 9 - Laminar Flow”. In: *Fluid Mechanics (Sixth Edition)*. Ed. by Pijush K. Kundu, Ira M. Cohen, and David R. Dowling. Sixth Edition. Boston: Academic Press, 2016, pp. 409 –467. ISBN: 978-0-12-405935-1.
- [Kel+08] Arnold J Kell, Gale Stewart, Shannon Ryan, Regis Peytavi, Maurice Boissinot, Ann Huletsky, Michel G Bergeron, and Benoit Simard. “Vancomycin-modified nanoparticles for efficient targeting and pre-concentration of Gram-positive and Gram-negative bacteria”. In: *Acs Nano* 2.9 (2008), pp. 1777–1788.
- [Kim+08] Min-Cheol Kim, Zhanhui Wang, Raymond H. W. Lam, and Todd Thorsen. “Building a better cell trap: Applying Lagrangian modeling to the design of microfluidic devices for cell biology”. In: *Journal of Applied Physics* 103.4 (2008), p. 044701. DOI: 10.1063/1.

2840059. eprint: <https://doi.org/10.1063/1.2840059>. URL: <https://doi.org/10.1063/1.2840059>.
- [Kiw+03] Toshihiko Kiwa, Masayoshi Tonouchi, Masatsugu Yamashita, and Kodo Kawase. “Laser terahertz-emission microscope for inspecting electrical faults in integrated circuits”. In: *Optics letters* 28.21 (2003), pp. 2058–2060.
- [Kiw+07] Toshihiko Kiwa, J Kondo, S Oka, I Kawayama, H Yamada, M Tonouchi, and Keiji Tsukada. “Laser-Terahertz Emission Readout of Chemical Sensors”. In: *TRANSDUCERS 2007-2007 International Solid-State Sensors, Actuators and Microsystems Conference*. IEEE. 2007, pp. 1915–1918.
- [Kiw+19] Toshihiko Kiwa, Tatsuki Kamiya, Taiga Morimoto, Kentaro Fujiwara, Yuki Maeno, Yuki Akiwa, Masahiro Iida, Taihei Kuroda, Kenji Sakai, Hidetoshi Nose, et al. “Imaging of chemical reactions using a terahertz chemical microscope”. In: *Photonics*. Vol. 6. 1. Multidisciplinary Digital Publishing Institute. 2019, p. 10.
- [KST13] Toshihiko Kiwa, Kenji Sakai, and Keiji Tsukada. “Imaging chemical reactions”. In: *SPIE Newsroom* (2013). URL: ,<https://doi.org/10.1117/2.1201312.005281>.
- [Lin+16] Samuel J Ling, Jeff Sanny, William Moebs, Gerald Friedman, Stphen D Druger, Alice Kolakowska, David Anderson, Daniel Bowman, Dedra Demaree, Edw Ginsberg, et al. “University Physics: OpenStax, Volume 1, ch:14”. In: (2016).

- [Liu+13] Zongbin Liu, Fei Huang, Jinghui Du, Weiliang Shu, Hongtao Feng, Xiaoping Xu, and Yan Chen. “Rapid isolation of cancer cells using microfluidic deterministic lateral displacement structure”. In: *Biomicrofluidics* 7.1 (2013), p. 011801. DOI: 10.1063/1.4774308. eprint: <https://doi.org/10.1063/1.4774308>. URL: <https://doi.org/10.1063/1.4774308>.
- [Mat13] John E Matsson. *An Introduction to SolidWorks Flow Simulation 2013*. SDC publications, 2013.
- [MH02] Deirdre R Meldrum and Mark R Holl. “Microscale bioanalytical systems”. In: *Science* 297.5584 (2002), pp. 1197–1198.
- [MT17] Despina Moschou and Angeliki Tserepi. “The lab-on-PCB approach: tackling the TAS commercial upscaling bottleneck”. In: *Lab Chip* 17 (8 2017), pp. 1388–1405. DOI: 10.1039/C7LC00121E. URL: <http://dx.doi.org/10.1039/C7LC00121E>.
- [NP+17] Hai Huy Nguyen Pham, Shintaro Hisatake, Oleg Vladilenovich Minin, Tadao Nagatsuma, and Igor Vladilenovich Minin. “Enhancement of spatial resolution of terahertz imaging systems based on terajet generation by dielectric cube”. In: *APL Photonics* 2.5 (2017), p. 056106. DOI: 10.1063/1.4983114. eprint: <https://doi.org/10.1063/1.4983114>. URL: <https://doi.org/10.1063/1.4983114>.
- [Oh+12] Kwang W Oh, Kangsun Lee, Byungwook Ahn, and Edward P Furlani. “Design of pressure-driven microfluidic networks using electric circuit analogy”. In: *Lab on a Chip* 12.3 (2012), pp. 515–545.

- [Ola+18] Ayokunle Olanrewaju, Maiwenn Beaugrand, Mohamed Yafia, and David Juncker. “Capillary microfluidics in microchannels: from microfluidic networks to capillaric circuits”. In: *Lab Chip* 18 (16 2018), pp. 2323–2347. DOI: 10.1039/C8LC00458G. URL: <http://dx.doi.org/10.1039/C8LC00458G>.
- [Par+17] Myoung-Hwan Park, Eduardo Reategui, Wei Li, Shannon N Tessier, Keith HK Wong, Anne E Jensen, Vishal Thapar, David Ting, Mehmet Toner, Shannon L Stott, et al. “Enhanced isolation and release of circulating tumor cells using nanoparticle binding and ligand exchange in a microfluidic chip”. In: *Journal of the American Chemical Society* 139.7 (2017), pp. 2741–2749.
- [PMW09] Emma Pickwell-MacPherson and Vincent P. Wallace. “Terahertz pulsed imaging—A potential medical imaging modality?” In: *Photodiagnosis and Photodynamic Therapy* 6.2 (2009), pp. 128 –134. ISSN: 1572-1000. DOI: <https://doi.org/10.1016/j.pdpdt.2009.07.002>. URL: <http://www.sciencedirect.com/science/article/pii/S1572100009000611>.
- [PPUn a] Roger Hinrichs Paul Peter Urone. *College Physics*. Houston, Texas: OpenStax, Jun 21, 2012. URL: <https://openstax.org/books/college-physics/pages/12-4-viscosity-and-laminar-flow-poiseuilles-law>.
- [PPUn b] Roger Hinrichs Paul Peter Urone. *College Physics*. Houston, Texas: OpenStax, Jun 21, 2012. URL: <https://openstax.org/books/college-physics/pages/12-1-flow-rate-and-its-relation-to-velocity>.

- [PZ15] Edward P.J. Parrott and J. Axel Zeitler. “Terahertz Time-Domain and Low-Frequency Raman Spectroscopy of Organic Materials”. In: *Applied Spectroscopy* 69.1 (2015). PMID: 25506684, pp. 1–25. DOI: 10.1366/14-07707. eprint: <https://doi.org/10.1366/14-07707>. URL: <https://doi.org/10.1366/14-07707>.
- [Sai+11a] Laure Saias, Julien Autebert, Laurent Malaquin, and Jean-Louis Viovy. “Design, modeling and characterization of microfluidic architectures for high flow rate, small footprint microfluidic systems”. In: *Lab on a Chip* 11.5 (2011), pp. 822–832.
- [Sai+11b] Laure Saias, Julien Autebert, Laurent Malaquin, and Jean-Louis Viovy. “Design, modeling and characterization of microfluidic architectures for high flow rate, small footprint microfluidic systems”. In: *Lab Chip* 11 (5 2011), pp. 822–832. DOI: 10.1039/COLC00304B. URL: <http://dx.doi.org/10.1039/COLC00304B>.
- [Sal+10] Antoine-Emmanuel Saliba, Laure Saias, Eleni Psychari, Nicolas Minc, Damien Simon, François-Clément Bidard, Claire Mathiot, Jean-Yves Pierga, Vincent Fraisier, Jean Salamero, et al. “Microfluidic sorting and multimodal typing of cancer cells in self-assembled magnetic arrays”. In: *Proceedings of the National Academy of Sciences* 107.33 (2010), pp. 14524–14529.
- [SLL14] Feng Shen, XiuJun Li, and Paul C. H. Li. “Study of flow behaviors on single-cell manipulation and shear stress reduction in microfluidic chips using computational fluid dynamics simulations”. In: *Biomicrofluidics* 8.1 (2014), p. 014109. DOI: 10.1063/1.4866358. eprint: <https://doi.org/10.1063/1.4866358>. URL: <https://doi.org/10.1063/1.4866358>.

- [Slo+05] Marcela Slováková, Nicolas Minc, Zuzana Bilková, Claire Smadja, Wolfgang Faigle, Claus Fütterer, Myriam Taverna, and Jean-Louis Viovy. “Use of self assembled magnetic beads for on-chip protein digestion”. In: *Lab on a Chip* 5.9 (2005), pp. 935–942.
- [SSW15] Dassault Systèmes SolidWorks, W Street, and M Waltham. “SOLIDWORKS 2016”. In: *Online help, Accessed* (2015), pp. 03–20.
- [Sta+20] Rayko Ivanov Stantchev, Xiao Yu, Thierry Blu, and Emma Pickwell-MacPherson. “Real-time terahertz imaging with a single-pixel detector”. In: *Nature communications* 11.1 (2020), pp. 1–8.
- [Sun+13] Jiashu Sun, Chao Liu, Mengmeng Li, Jidong Wang, Yunlei Xianyu, Guoqing Hu, and Xingyu Jiang. “Size-based hydrodynamic rare tumor cell separation in curved microfluidic channels”. In: *Biomicrofluidics* 7.1 (2013), p. 011802. DOI: 10.1063/1.4774311. eprint: <https://doi.org/10.1063/1.4774311>. URL: <https://doi.org/10.1063/1.4774311>.
- [SW03] Samuel K Sia and George M Whitesides. “Microfluidic devices fabricated in poly (dimethylsiloxane) for biological studies”. In: *Electrophoresis* 24.21 (2003), pp. 3563–3576.
- [Ton07] Masayoshi Tonouchi. “Cutting-edge terahertz technology”. In: *Nature photonics* 1.2 (2007), pp. 97–105.
- [Tor+20] Juan F Torres, Yongling Zhao, Shuqi Xu, Zhengyu Li, and Atsuki Komiya. “Optical Method for Simultaneous High-Resolution Measurement of Heat and Fluid Flow: The Case of Rayleigh-Bénard Convection”. In: *Physical Review Applied* 14.5 (2020), p. 054038.

- [UH+18] Paul Peter Urone, Roger Hinrichs, et al. “College Physics: OpenStax”. In: (2018).
- [Ver02] Elisabeth Verpoorte. “Microfluidic chips for clinical and forensic analysis”. In: *Electrophoresis* 23.5 (2002), pp. 677–712.
- [Ver+14] Marie Versaevel, Thomas Grevesse, Maryam Riaz, Joséphine Lantoine, and Sylvain Gabriele. “Chapter 3 - Micropatterning HydroxyPAAm Hydrogels and Sylgard 184 Silicone Elastomers with Tunable Elastic Moduli”. In: *Micropatterning in Cell Biology Part C*. Ed. by Matthieu Piel and Manuel Théry. Vol. 121. Methods in Cell Biology. Academic Press, 2014, pp. 33 –48. DOI: <https://doi.org/10.1016/B978-0-12-800281-0.00003-8>. URL: <http://www.sciencedirect.com/science/article/pii/B9780128002810000038>.
- [Wan+18] Renjie Wang, Yi Xu, Thomas Sors, Joseph Irudayaraj, Wen Ren, and Rong Wang. “Impedimetric detection of bacteria by using a microfluidic chip and silver nanoparticle based signal enhancement”. In: *Microchimica Acta* 185.3 (2018), p. 184.
- [Xu+13] Xiaoxiao Xu, Pinaki Sarder, Zhenyu Li, and Arye Nehorai. “Optimization of microfluidic microsphere-trap arrays”. In: *Biomicrofluidics* 7.1 (2013), p. 014112. DOI: 10.1063/1.4793713. eprint: <https://doi.org/10.1063/1.4793713>. URL: <https://doi.org/10.1063/1.4793713>.
- [YA12] Shahrzad Yazdi and Arezoo M. Ardekani. “Bacterial aggregation and biofilm formation in a vortical flow”. In: *Biomicrofluidics* 6.4 (2012), p. 044114. DOI: 10.1063/1.4771407. eprint: <https://doi.org/10.1063/1.4771407>.

- doi.org/10.1063/1.4771407. URL: <https://doi.org/10.1063/1.4771407>.
- [Yam+05] Masatsugu Yamashita, Kodo Kawase, Chiko Otani, Toshihiko Kiwa, and Masayoshi Tonouchi. “Imaging of large-scale integrated circuits using laser terahertz emission microscopy”. In: *Optics Express* 13.1 (2005), pp. 115–120.
- [Yan+16] Xiang Yang, Xiang Zhao, Ke Yang, Yueping Liu, Yu Liu, Weiling Fu, and Yang Luo. “Biomedical Applications of Terahertz Spectroscopy and Imaging”. In: *Trends in Biotechnology* 34.10 (2016), pp. 810 –824. ISSN: 0167-7799. DOI: <https://doi.org/10.1016/j.tibtech.2016.04.008>. URL: <http://www.sciencedirect.com/science/article/pii/S0167779916300270>.
- [YII18] “7 - Microfluidic Devices Based on Biomechanics”. In: *Integrated Nano-Biomechanics*. Ed. by Takami Yamaguchi, Takuji Ishikawa, and Yohsuke Imai. Micro and Nano Technologies. Boston: Elsevier, 2018, pp. 217 –263. ISBN: 978-0-323-38944-0. DOI: <https://doi.org/10.1016/B978-0-323-38944-0.00007-3>. URL: <http://www.sciencedirect.com/science/article/pii/B9780323389440000073>.
- [ZH19] John X.J. Zhang and Kazunori Hoshino. “Chapter 3 - Microfluidics and micro total analytical systems”. In: *Molecular Sensors and Nanodevices (Second Edition)*. Ed. by John X.J. Zhang and Kazunori Hoshino. Second Edition. Micro and Nano Technologies. Academic Press, 2019, pp. 113 –179. ISBN: 978-0-12-814862-4. DOI: <https://doi.org/10.1016/B978-0-12-814862-4.00003-X>.

URL: <http://www.sciencedirect.com/science/article/pii/B978012814862400003X>.

- [Zho+19] Hong Zhou, Cheng Yang, Donglin Hu, Dongxiao Li, Xindan Hui, Feng Zhang, Ming Chen, and Xiaojing Mu. “Terahertz biosensing based on bi-layer metamaterial absorbers toward ultra-high sensitivity and simple fabrication”. In: *Applied Physics Letters* 115.14 (2019), p. 143507. DOI: 10.1063/1.5111584. eprint: <https://doi.org/10.1063/1.5111584>. URL: <https://doi.org/10.1063/1.5111584>.

Index

- AD converter, 5, 16
- AD filter, 5
- ANSYS Simulator, 7
- ANSYS simulator, 48
- Average THz data, 16
- average velocity, 40
- CCD camera, 4
- CFD simulator, 43
- Contrast, 5
- Cylindrical path, 8
- DPM, 15
- femtosecond laser, 12
- Imaging noise, 5
- LabVIEW, 16
- laminar, 7, 48
- lock-in-amplifier, 5
- LTME, 3
- microfluidic chip, 6
- microfluidics, 2
- NDT, 3
- PDMS, 6, 20
- Rectangular path, 8
- Regression method, 51
- Reynold number, 8
- SFG, 16
- Solid work, 20
- TDS, 3
- Terahertz, 1
- THz detection, 15
- THz detector, 16
- THz generation, 13
- Ti:Sapphire laser, 15
- VOF, 45

Biography

Feroz Ahmed was born in 1985 in a clam and quiet village in Bangladesh. He received the Bachelor (B.Sc.) degree in Electrical and Engineering from Khulna University of Engineering and Technology (KUET), Bangladesh in 2007. In 2008, he joined Prime University of Bangladesh as a full time lecturer, he worked as a lecturer from 2008 to 2011, senior lecturer from 2011 to 2012, and he left his job for pursuing his higher study in Barcelona, Spain. In Spain, he received his Masters degree in Photonics from Polytechnic University of Catalonia (UPC), Barcelona in 2013. Then he worked as a Photovoltaic Engineer under the Hi-VAN Bangladesh Ltd. of Barcelona, Spain branch till the year of 2017. Now he has been pursuing his Ph.D. degree in the field of Medical Bioengineering at Okayama University under the supervision of Professor Toshihiko Kiwa since October, 2017. He awarded the Otsuka Toshimi Scholarship in 2018 to pursue his Ph.D. degree. His research interest includes microfluidics, fluid dynamics, THz image sensing, optical biosensing and digital signal processing.